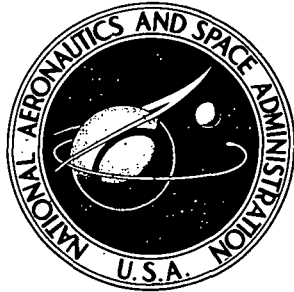


NASA CR-2381

NASA CONTRACTOR
REPORT



NASA CR-2381

AN EXPERIMENTAL STUDY
OF THE VALIDITY OF
THE HEAT-FIELD CONCEPT
FOR SONIC-BOOM ALLEVIATION

by Rudolph J. Swigart

Prepared by
THE AEROSPACE CORPORATION
El Segundo, Calif.
for Langley Research Center

NATIONAL AERONAUTICS AND SPACE ADMINISTRATION • WASHINGTON, D. C. • MARCH 1974

1. Report No. NASA CR-2381	2. Government Accession No.	3. Recipient's Catalog No.	
4. Title and Subtitle AN EXPERIMENTAL STUDY OF THE VALIDITY OF THE HEAT-FIELD CONCEPT FOR SONIC-BOOM ALLEVIATION		5. Report Date March 1974	
7. Author(s) Rudolph J. Swigart		6. Performing Organization Code	
9. Performing Organization Name and Address The Aerospace Corporation El Segundo, California		8. Performing Organization Report No. ATR-74 (7218)-1	
12. Sponsoring Agency Name and Address National Aeronautics and Space Administration Washington, D.C. 20546		10. Work Unit No. 126-13-11-01-00 760-74-01-04-00	
		11. Contract or Grant No. NAS 1-10051	
		13. Type of Report and Period Covered Contractor Report	
		14. Sponsoring Agency Code	
15. Supplementary Notes This is a final report.			
16. Abstract An experimental program was carried out in the NASA-Langley 4 ft x 4 ft supersonic pressure tunnel to investigate the validity of the heat-field concept for sonic-boom alleviation. The concept involves heating the flow about a supersonic aircraft in such a manner as to obtain an increase in effective aircraft length and yield an effective aircraft shape that will result in a shock-free pressure signature on the ground.			
<p>First, a basic body-of-revolution representing an SST configuration with its lift equivalence in volume was tested to provide a baseline pressure signature. Second, a model having a 5/2-power area distribution which, according to theory, should yeild a linear pressure rise with no front shock wave was tested. Third, the concept of providing the 5/2-power area distribution by using an off-axis slender fin below the basic body was investigated. Then a substantial portion (approximately 40 percent) of the solid fin was replaced by a heat field generated by passing heated nitrogen through the rear of the fin.</p> <p>In general the measured pressure signatures agreed well with theoretical predictions. Comparisons of pressure signatures for the thermal-fin model with no flow, cold flow, and heated flow through the fin demonstrated substantial effects due to flow and due to heat, essentially verifying the use of mass flow and heat fields for providing equivalent area in supersonic flow and creating shockless signatures.</p>			
17. Key Words (Suggested by Author(s)) Sonic Boom, Sonic Boom Minimization, Aircraft Design, Noise Suppression		18. Distribution Statement Unclassified-Unlimited	
19. Security Classif. (of this report) Unclassified		20. Security Classif. (of this page) Unclassified	
		21. No. of Pages 78	22. Price* \$3.75

CONTENTS

SUMMARY	1
INTRODUCTION	2
SYMBOLS	5
1. TEST FACILITY	8
2. TEST MODELS AND MODEL DESIGN	8
3. RESULTS AND DISCUSSION	20
4. CONCLUSIONS	40
5. SUGGESTED FUTURE RESEARCH	40
APPENDICES:	
A. DESIGN EQUATIONS FOR BASIC BODY, FRONTAL SPIKE, SOLID FIN, THERMAL FIN, AND WING-BODY MODELS	43
B. THERMAL FIN MODEL NOZZLE DESIGN ANALYSIS	59
C. HEATING-TUBE ANALYSIS-DETERMINATION OF NOZZLE MASS-FLOW RATE	63
D. DESCRIPTION OF CONTROL CONSOLE	67
REFERENCES	73

FIGURES

1.	Signature of Supersonic Aircraft	3
2.	Wind-Tunnel Test Section Apparatus and Nomenclature	9
3.	Basic Body of Revolution Representing Typical SST Configuration	10
4.	Effective Area Distributions for the Basic Body	11
5.	5/2-Power Body Frontal Spike	12
6.	Effective Area Distribution for the 5/2-Power Body	13
7.	Solid Fin Model	15
8.	Twin-Body Model	16
9.	Thermal Fin Model	17
10.	Thermal-Fin Model Cross Section	18
11.	Thermal-Fin Mach-Plane Area Distribution	19
12.	Wing-Body Model	21
13.	Comparison of Experimental and Theoretical Pressure Distributions (Basic Body)	22
14.	Comparison of Experimental and Theoretical Pressure Distributions (Basic Body)	23
15.	Comparison of Experimental and Theoretical Pressure Distributions (Frontal Spike)	24
16.	Comparison of Experimental and Theoretical Pressure Distributions (Frontal Spike)	25
17.	Comparison of Experimental and Theoretical Pressure Distributions (Solid Fin Model)	27
18.	Comparison of Experimental and Theoretical Pressure Distributions (Solid Fin Model)	28
19.	Comparison of Experimental and Theoretical Pressure Distributions (Twin-Body Model)	29
20.	Comparison of Experimental and Theoretical Pressure Distributions (Twin-Body Model)	30
21.	Comparison of Experimental and Theoretical Pressure Distributions (Twin-Body Model)	31
22.	Comparison of Experimental and Theoretical Pressure Distributions (Twin-Body Model)	32
23.	Experimental Pressure Distributions	34
24.	Comparison of Experimental and Theoretical Pressure Distributions (Thermal Fin)	35

FIGURES (Continued)

25.	Experimental Pressure Distribution (Thermal Fin)	36
26.	Comparison of Experimental and Theoretical Pressure Distributions (Thermal Fin)	37
27.	Comparison of Experimental and Theoretical Pressure Distributions (Thermal Fin)	38
28.	Comparison of Experimental and Theoretical Pressure Distributions (Wing-Body)	39
29.	Comparison of Experimental and Theoretical Pressure Distributions (Wing-Body with Solid Fin).	41
30.	Sonic-Boom Control Console	68
31.	Sonic-Boom Test Console Schematic	69
32.	Sonic-Boom Test Console Legend and Operating Instructions	70

AN EXPERIMENTAL STUDY OF THE VALIDITY OF THE
HEAT-FIELD CONCEPT FOR
SONIC-BOOM ALLEVIATION

by Rudolph J. Swigart
The Aerospace Corporation

SUMMARY

An experimental program was carried out in the NASA-Langley 4 ft x 4 ft supersonic pressure tunnel to investigate the validity of the heat-field concept for sonic-boom alleviation. The basic idea of the heat-field concept is to heat the flow about a supersonic aircraft in such a manner as to obtain an increase in effective aircraft length and yield an effective aircraft shape (area distribution) that will result in a shock-free pressure signature on the ground. By eliminating the shock waves in the classical N-wave sonic-boom signature, a substantial reduction in sonic-boom noise heard out-of-doors can be achieved.

In the experimental program, seven 1/360-scale wind-tunnel models were tested to provide a step-by-step verification of the heat-field concept. First, a basic body-of-revolution with its lift equivalence in volume was tested to provide a baseline pressure signature containing front and rear shock waves. Second, a model having a 5/2-power area distribution was tested which, according to theory, should yield a linear pressure rise with no front shock wave. Third, the concept of providing the 5/2-power area distribution by using either an off-axis slender fin below the basic body or an additional body of revolution, area-ruled such that the total areas of the basic body and the fin or additional body have the same Mach-plane area distribution as the 5/2-power spike, was investigated. Then, to investigate the use of a heat field for providing effective body shapes in supersonic flow, a substantial portion (approximately 40 percent) of the solid fin was replaced by a heat field generated by passing heated nitrogen through the rear of the fin.

In addition to the above tests, the ability of the off-axis fin to produce a finite rise-time signature in the presence of lift was investigated by testing a wing-body model both with and without the solid fin previously tested in conjunction with the basic body.

The measured pressure signatures agreed well with theoretical predictions, with the exception of the signatures for the dual body-of-revolution model area-ruled to have the same signature as the 5/2-power frontal spike. This model exhibited a strong compression off the nose of the upper body that could not be eliminated by compensating expansions from the lower body. Comparisons of pressure signatures for the thermal-fin model with no flow, cold flow, and heated flow through the fin demonstrated substantial effects due to flow and due to heat, essentially verifying the use of mass flow and heat fields for providing equivalent area in supersonic flow. Moreover, the results for the wing-body with solid fin model clearly demonstrated the effectiveness of the fin in producing a finite rise-time signature in the presence of lift.

INTRODUCTION

An aircraft in supersonic flight generates a complex pressure field that simplifies as it propagates, giving rise to the so-called sonic boom (fig. 1). The far-field signature is typically N-shaped, being characterized by two shock waves separated by a linear expansion. For current-generation aircraft of the supersonic transport (SST) class, it is estimated that the reflected shock strength will be on the order of 100-200 N/m² (2-4 psf) during cruise conditions.

The principal aspects of the sonic boom causing public concern are structural damage and noise. Based on extensive studies of the structural damage question, relatively few structures will be damaged by booms having overpressures below about 250 N/m² (5 psf) (ref. 1). Thus, it appears that adverse public reaction is associated mainly with the acoustic effects of the boom. A substantial startle effect is produced by a shock having an overpressure of the order of 100 N/m² or more, and this gives rise to annoyance.

The question, however, of what constitutes an acceptable sonic-boom pressure signature is unanswered at this time (ref. 2). It is known that replacement of the front and rear shock waves in the classical N-wave sonic-boom signature by pressure increments occurring over times as small as 10 msec results in a substantial reduction of acoustic power in the frequencies to which the ear is most sensitive, thereby reducing the outdoor annoyance of the boom (refs. 1 and 3). Studies to determine the optimal configuration and minimum length for an aircraft having a signature without shock waves have been undertaken by a number of investigators over the past several years (refs. 2, 4, 5, 6) with a closed-form result evolving only recently (refs. 2, 4). These results yield a required length of 173.74 m (570 ft) for an SST-type aircraft with a gross weight of 272,155 kg (600,000 lbm) flying at an altitude of 18,288 m (60,000 ft) at Mach 2.7. Although this length is substantially below earlier estimates of about 304.8 m (1000 ft) (ref. 6), it is still beyond that generally considered feasible for practical implementation. Consequently, consideration has been given to the possible use of heat or force fields distributed about the aircraft in such a manner as to create a so-called "phantom body" having the length and area distribution required to produce a bangless-boom signature.

Several investigator's have examined heat and force-field concepts and have made estimates of the power requirements and weight penalties associated with their implementation (refs. 1, 7, 8, 9). Cheng and Goldburg (ref. 7), upon close examination of the use of electro-aerodynamic techniques to reduce the sonic boom as first proposed by Cahn and Andrew (ref. 10), concluded that on the order of 454,000 kg (1,000,000 lb) of electrical equipment would be required to generate the power needed to reduce the overpressure of the leading shock wave in the sonic-boom signature by ten percent. Both Batdorf (ref. 1) and Miller and Carlson (ref. 8), considering a heat field generated by direct combustion of the same fuel as used by the main SST engines, concluded that the front shock wave could be eliminated through properly

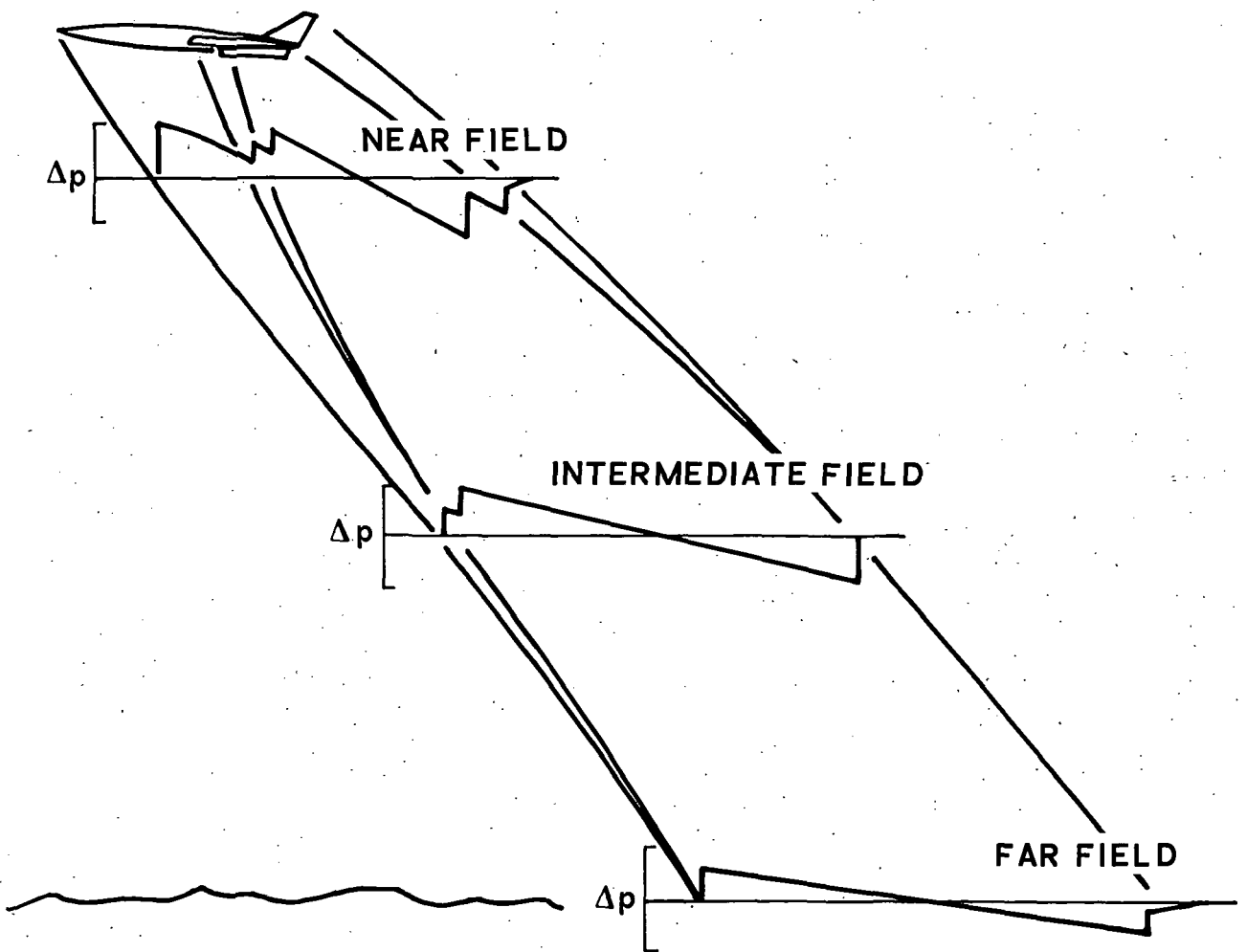


Figure 1. Signature of Supersonic Aircraft

controlled burning of an amount of fuel corresponding to about 20 percent of that normally carried to meet propulsion needs. On consideration of rear shock elimination also, Miller and Carlson concluded that this penalty would increase to about 60 percent additional on-board fuel with no account taken of the weight and performance penalties of the system. Lipfert (ref. 9) predicted the weight penalty associated with alleviation devices in terms of additional structural weight and additional fuel weight for both shock-wave elimination and to overcome the additional drag due to the additional weight. He considered the use of hydrogen (a pollution-free fuel) as well as hydrocarbon fuels not only for shock elimination but also to supply the propulsive power to overcome the drag penalty. The minimum weight penalty to remove both the front and rear shocks for 272,155 kg (600,000 lbm) aircraft flying a 5000-second mission at Mach 2.7 at an altitude of 18,898 m (62,000 ft) was estimated to be 226.796 kg (500,000 lbm). These tentative conclusions indicate a questionable practicality of using free combustion to remove both front and rear shocks. However, the use of free combustion in conjunction with other ideas, such as the use of a high tail to obtain, in the area-rule sense, the required additional length needed to remove the rear shock wave (e.g., ref. 11), could bring such concepts back into the realm of practicality. In implementation of these concepts employment of the area rule allows off-axis combustion to be considered (refs. 1, 8). This has particular attraction in the case of the front shock, since it replaces the difficult problem of burning against the flow ahead of the aircraft with one of burning in the direction of flow beneath the aircraft.

Questions concerned with the engineering and economic feasibility of practical incorporation of the previously discussed design features in supersonic transport aircraft can be answered only after exhaustive studies by qualified design teams with representatives from all technology areas. However, there are rather fundamental questions concerning the validity of the heat-field concept than can be answered by means of properly conducted but relatively simple wind tunnel tests. Such is the purpose of the present investigation. To investigate the feasibility of using an off-axis heat field for removal of the leading shock wave in the sonic-boom signature, an experimental program was carried out in the NASA-Langley 4 ft x 4 ft supersonic pressure tunnel. Seven wind-tunnel models were tested and pressure signatures recorded at two and three body lengths in the plane directly below the aircraft. The results of these tests are reported herein.

The author would like to acknowledge the significant contributions of his colleagues at The Aerospace Corporation to this program. Dr. S. B. Batdorf provided overall supervision to the program and originated the basic concept that was investigated, i.e., the use of heat in an off-axis configuration such as a thermal fin; Mr. W. R. Grabowsky carried out the thermal analysis and preliminary design of the heating system incorporated in the thermal fin, and Mr. D. A. Durran transformed the preliminary design of all the models into detail designs and designed the power-supply console. All of the wind tunnel models were fabricated by the Laboratory Operations Machine Shop.

SYMBOLS

Dimensions of physical quantities are given in the International System of Units (SI). Equivalent values are indicated parenthetically in the U.S. Customary System. Details concerning the use of SI, together with physical constants and conversion factors, are given in reference 12.

A	area
AR	aspect ratio
C _L	lift coefficient
c _p	specific heat at constant pressure
D	heating-tube diameter
E	elliptic integral of the second kind
F(y)	Whitham F function, $\frac{1}{2\pi} \int_0^y \frac{A''(\xi)}{\sqrt{y-\xi}} d\xi$ where $A''(\xi)$ is the second derivative of the cross-sectional area distribution
h	static enthalpy; also convective heat-transfer coefficient
h(y)	fin width in maximum-thickness plane
I	current
K	constant in 5/2-power law body-shape equation
K _p	potential lift coefficient/ $\sin\alpha \cos^2\alpha$
K _v	vortex lift coefficient/ $\sin^2\alpha \cos\alpha$
k	$\frac{\gamma+1}{\sqrt{2}} \frac{M_\infty^4}{\beta^{3/2}}$; also thermal conductivity
L	longitudinal separation distance of bodies in twin-body model (fig. 6).
ℓ	various fin Mach-plane chord lengths, depending on subscript (Appendix A)
M	Mach number, also $m c_p / \rho D$
m	mass-flow rate; also parameter of elliptic integral of second kind

M. W.	molecular weight
P	$I^2 R / \pi D t$, electrical power per unit area of heating-tube wall
p	static pressure
Δp	difference between disturbance pressure caused by model and freestream static pressure
Pr	Prandtl number
q_c	convective heat-transfer rate
R	resistivity
r	perpendicular distance from model to measuring probe; also heater-tube radial variable
Re	Reynolds number
S	perpendicular separation distance of bodies in twin-body model (fig. 6); also heating-tube cross-sectional area
T	static temperature
T°	stagnation temperature
t	heating-tube wall thickness
V	velocity
w	fin trailing-edge width (Appendix A); also nozzle width (Appendix B)
x	distance measured along longitudinal axis from model nose; also distance along heating tube
y	vertical distance measured from tip of fin; also characteristic variable in Whitham theory (Appendix A)
α	angle of attack; also resistivity temperature-dependence coefficient
β	$\sqrt{M_\infty^2 - 1}$; also coefficient of temperature dependence of thermal conductivity
γ	specific-heat ratio
ϵ	emissivity
λ_{LE}	leading-edge sweep angle

μ Mach angle, $\sin^{-1} \frac{1}{M}$

ρ density

σ Stefan-Boltzmann constant

Subscripts

B basic body of revolution

b bulk

c centerline value

D based on heating-tube diameter

e effective or exit

F fin structure

H heat

j properties in nozzle jet at exit plane

L due to lift

o initial or entrance value

R reference condition

S 5/2-power frontal spike

w wall condition

μ in Mach planes

∞ free-stream value

1. TEST FACILITY

The tests were carried out in the NASA-Langley 4 ft x 4 ft supersonic pressure tunnel at a free-stream Mach number of 2.01 and total temperature of 317°K (570°R). All of the tests were performed at a tunnel stagnation pressure of 69 kN/m² (10 psia) with the exception of two signatures for the thermal-fin model that were taken at a tunnel stagnation pressure of 51.7 kN/m² (7.5 psia). Many tests in which sonic-boom pressure signatures have been measured for both simple and complex configurations have been carried out in this facility, and high-resolution signatures have been obtained (refs. 13, 14, 15).

For the tests under consideration, the models were mounted on a remotely controlled actuator permitting their movement relative to a slender static-pressure probe (fig. 2). To obtain a signature, the probe position is held fixed in the tunnel and the model is moved forward relative to it. In this manner, the flow disturbances originating at different positions on the body always traverse the same region of flow between the body and probe, thereby having any free-stream flow nonuniformities in common. In this fashion, different points in the signature are referenced to a common base.

2. TEST MODELS AND MODEL DESIGN

Seven wind-tunnel models were tested during the course of the investigation. Detailed design rationale and mathematical description of the models are given in Appendix A. A basic body-of-revolution (fig. 3) having a nominal length of 25.4 cm (10 in.) was used to represent at 1/360 scale a typical SST configuration. Such a body provides a baseline signature containing front and rear shock waves. The basic-body area development was patterned on an SST area distribution taken from reference 6 and was modified slightly so that the front shock wave could be eliminated by heat addition only (i.e., no heat removal) (fig. 4). In this model, the lift is replaced by its equivalence in volume according to the rules of linearized theory (ref. 16). In addition, the nose of the model is modified to have a 5/2-power area distribution such that the front shock wave will not form within a distance of about 25 cm (10 in.) from the body (Appendix A). The reason for this is to allow the fin of the model discussed below to interact with the basic-body disturbances before nonlinear effects become important, thereby satisfying requirements for applicability of the supersonic area rule.

The second model tested is a body of revolution whose area grows as the 5/2-power distance from its nose (fig. 5). This is the minimum-length area distribution for a finite rise-time pressure signature, and is the distribution that will result in a linear pressure rise for the first compression in the signature according to the basic theory of Whitham (ref. 17). This model was designed to represent an airplane equivalent body with a full scale length of 152 m (500 ft), and be 61 m (200 ft) longer than the airplane itself (see fig. 6),

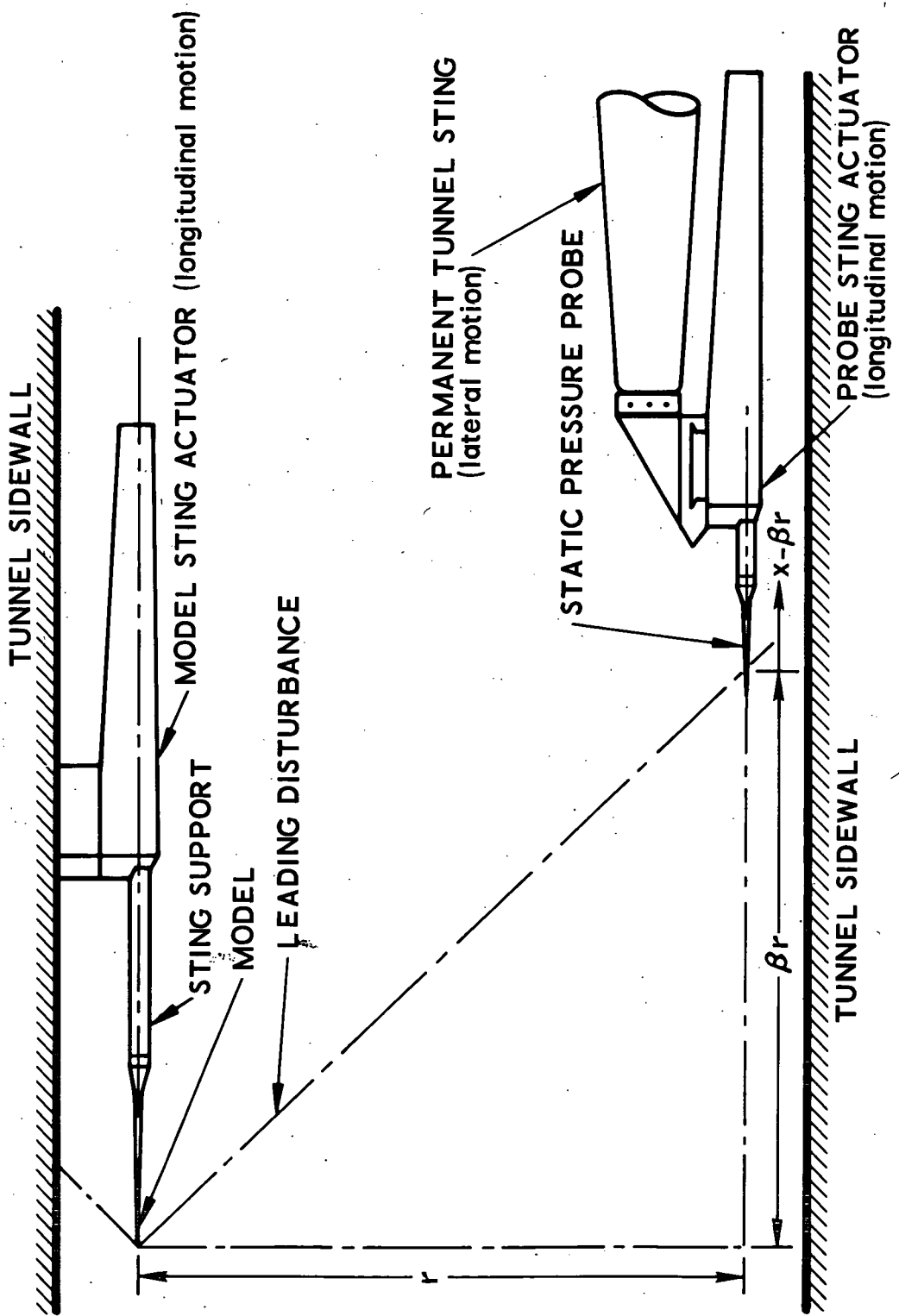
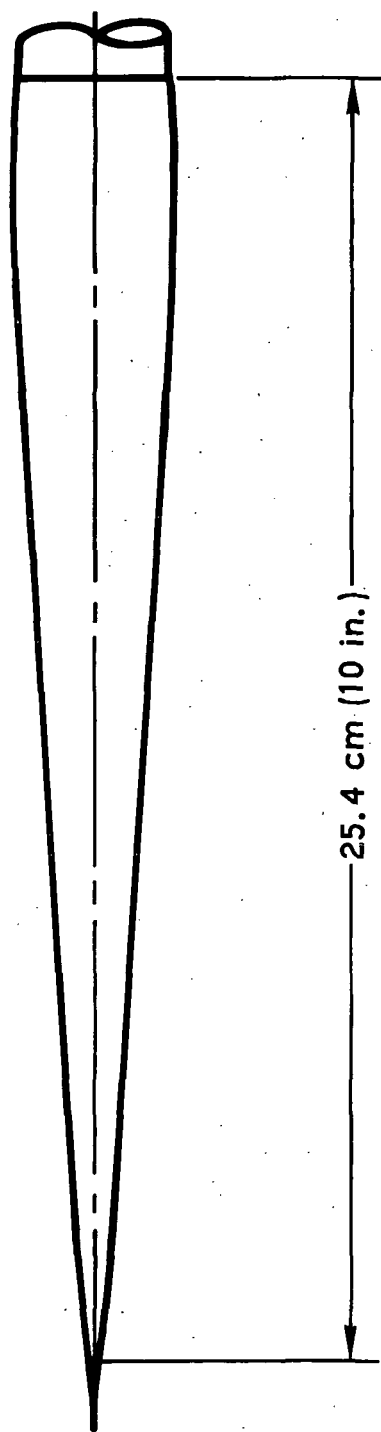


Figure 2. Wind-Tunnel Test Section Apparatus and Nomenclature

Figure 3. Basic Body of Revolution Representing
Typical SST Configuration



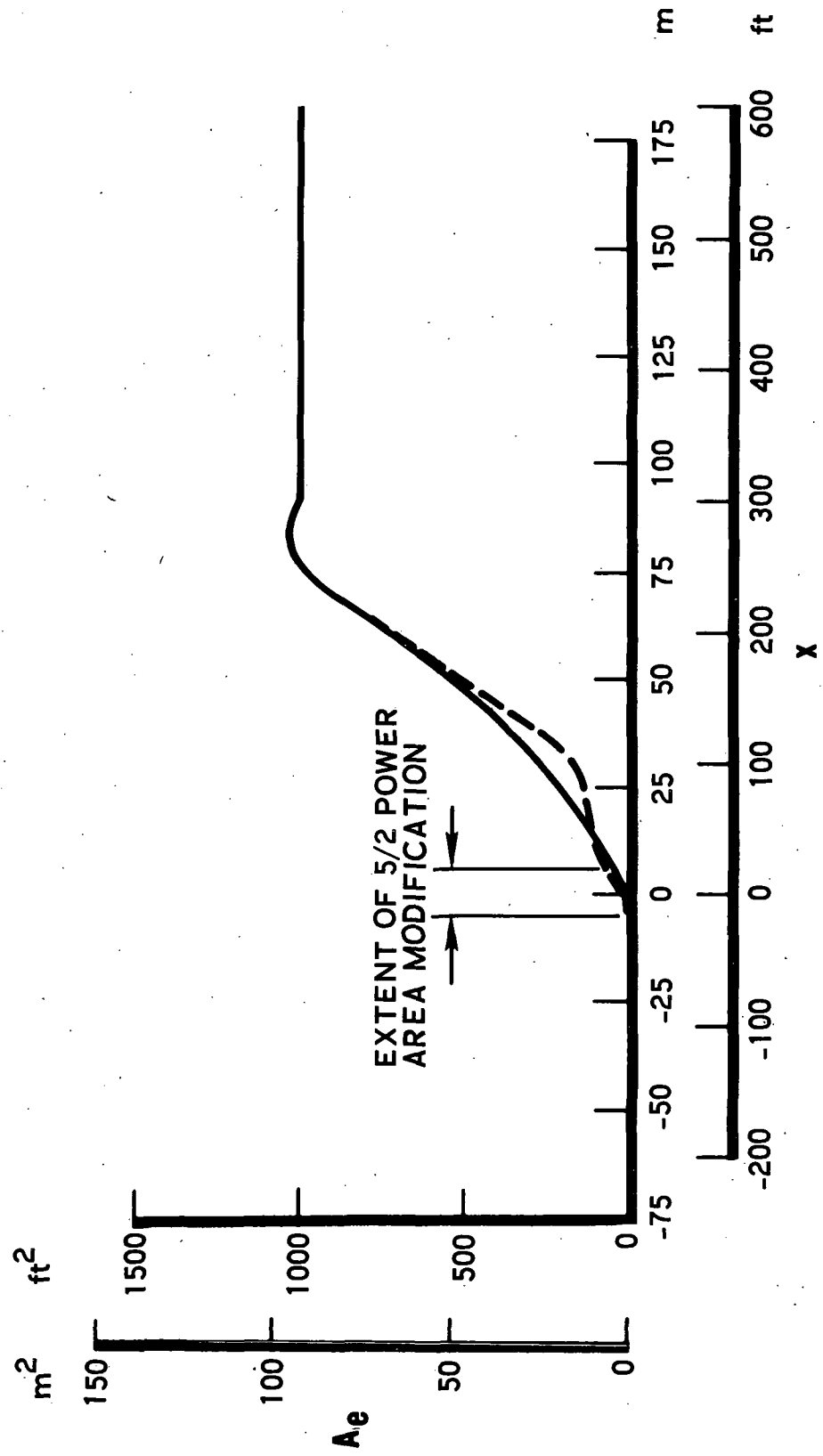
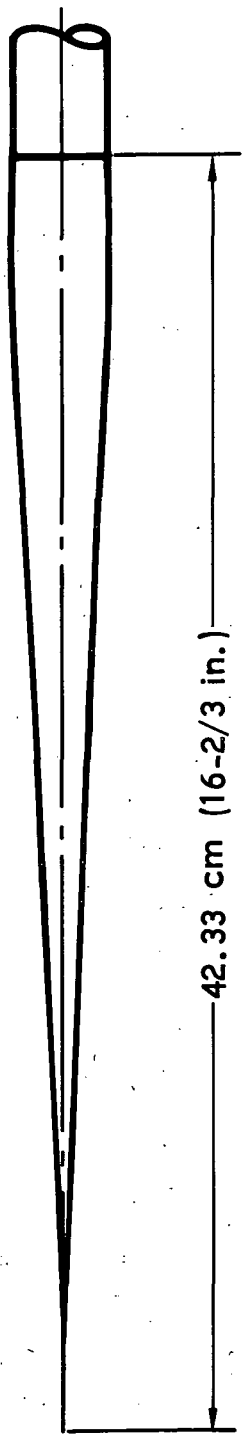


Figure 4. Effective Area Distributions for the Basic Body

Figure 5. 5/2-Power Body Frontal Spike



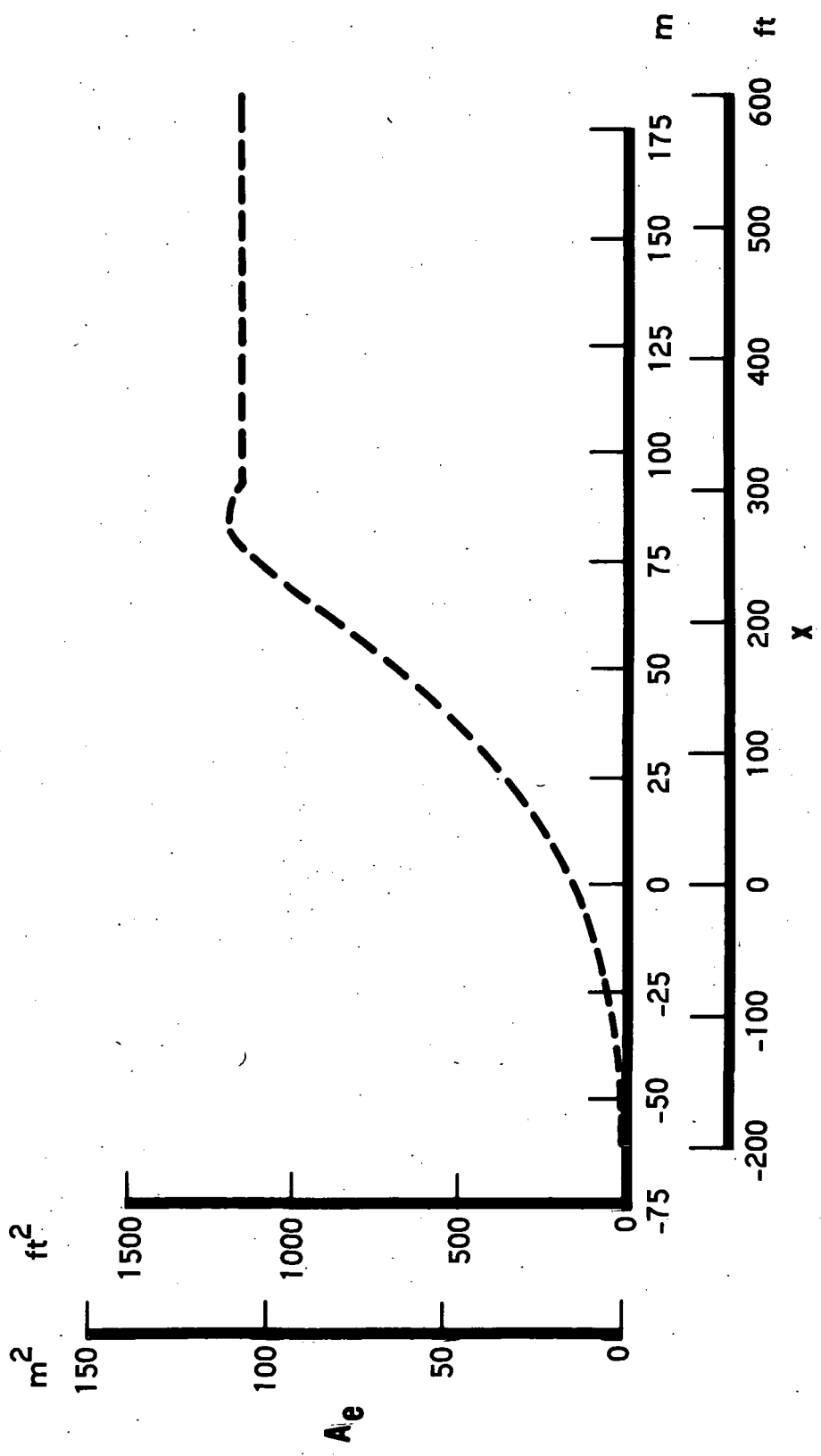


Figure 6. Effective Area Distribution for the
5/2-Power Body

and of such a contour that the area difference between the basic body and the 5/2-power frontal spike is constant aft of the nose of the basic body. This would correspond to the case of heat distributed upstream of the basic body in such a fashion as to displace streamlines in a manner identical to the 5/2-power frontal spike. The heating would end at the nose of the basic body (ref. 1).

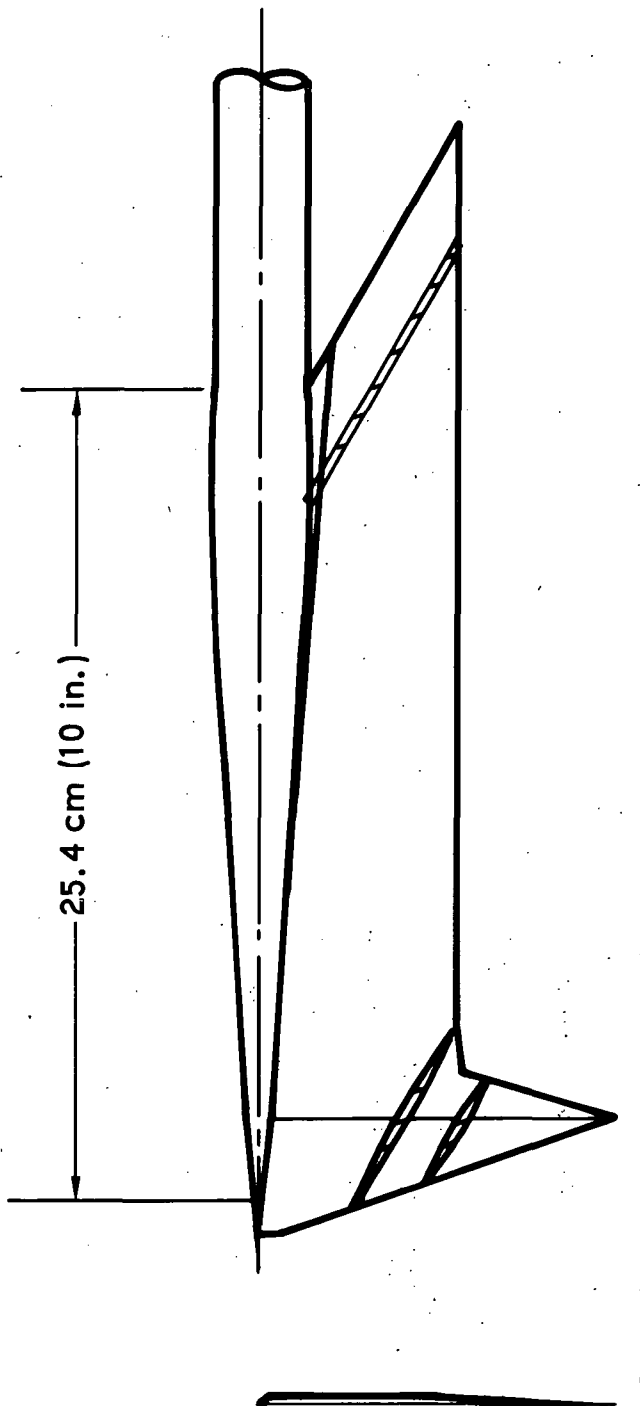
The third model incorporates a solid fin situated below the basic body of revolution and is designed so that the area distribution in Mach cutting planes perpendicular to the lateral symmetry plane of the fin is identical to that of the 5/2-power spike (fig. 7). The purpose of the 5/2-power area distribution nose on the basic body (discussed above) is to allow disturbances from the fin to interact with those from the basic body before nonlinear effects become important, thereby satisfying requirements for applicability of the supersonic area rule. The fin is designed to have a double-wedge cross-section in Mach planes, with a maximum front-wedge angle of four degrees in horizontal planes. It is necessary to keep the front wedge-angle in horizontal planes small in order to remain within the bounds of linearized theory, upon which the supersonic area rule is based (ref. 16). When these conditions are met, the pressure signature below the fin in the lateral symmetry plane of the fin is theoretically identical to that of the 5/2-power spike.

The fourth model tested is the so-called twin-body wherein a second body of revolution is situated below the basic body of revolution (fig. 8). The second body has a Mach-plane area distribution defined so that the sum of its area and that of the basic body is equal to the area distribution of the 5/2-power spike model. Again, according to the area rule, the pressure signatures of this model in the plane through both axes of the bodies of revolution should be identical to that of the 5/2-power body. The model is designed for separation distances, S , between the two bodies of 4.445 cm (1.75 in.) and 8.89 cm (3.50 in.) and variable relative length distances, L .

The fifth model tested is the thermal-fin model in which approximately 40 percent of the fin volume of Model 3 is replaced by a heat field designed to have the equivalent area distribution in Mach planes of the solid fin (fig. 9). The heat field is generated by passing nitrogen through a 0.3175-cm (1/8-in.) diameter heating tube that continues through the model into a nozzle whose exit plane is at the rear of the fin (fig. 10). In order to accommodate the 1/8-in. heating tube in the fin section, the scale of the thermal-fin model was increased by a factor of 1.5 over its solid counterpart. Hence, the basic-body portion of the thermal fin model has a nominal length of 38.1 cm (15 in.).

The thermal fin Mach-plane area distribution is shown in figure 11. In the Mach plane at the end of the heated region, better than 60 percent of the fin area is represented by heat. This percentage drops to 43 percent at 30.163 cm (11.875 in.) and remains constant thereafter. In terms of volume, about 40 percent of the total fin volume is represented by the heat field.

Details of the design of the thermal fin and heating tube are given in Appendices B and C.



FIN FRONTAL
VIEW

Figure 7. Solid Fin Model

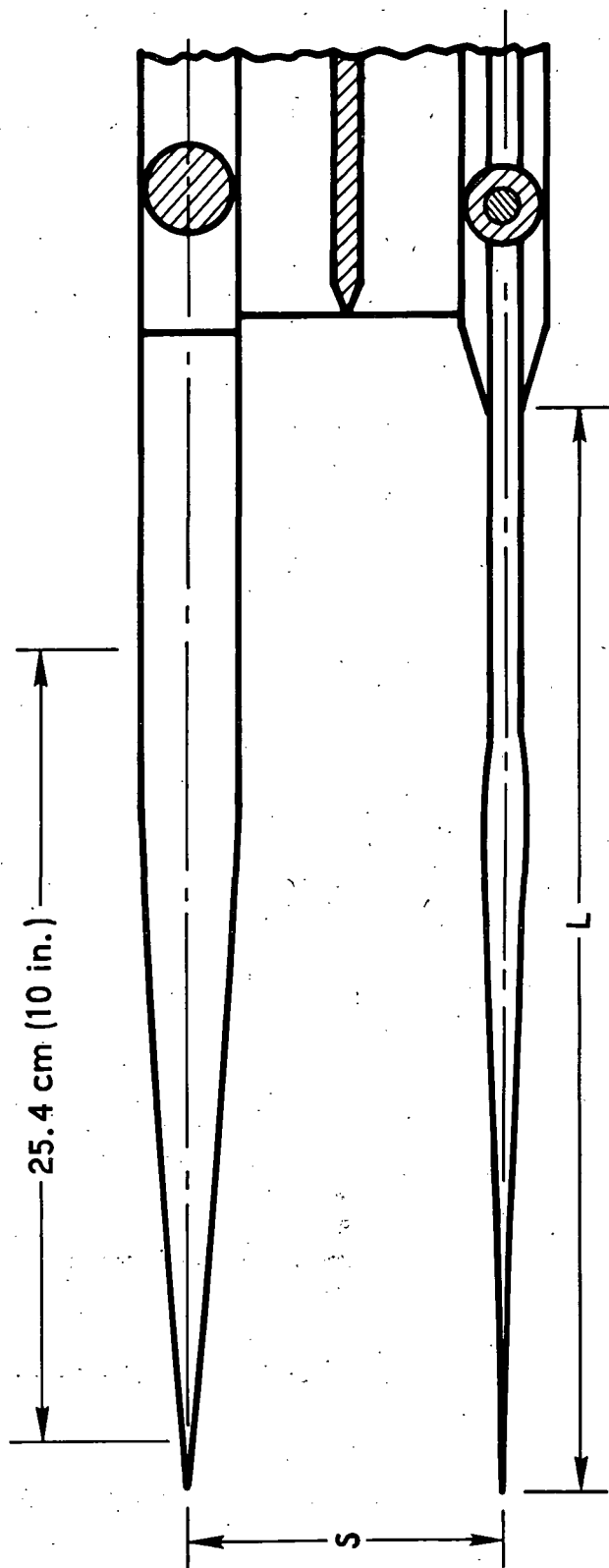


Figure 8. Twin-Body Model

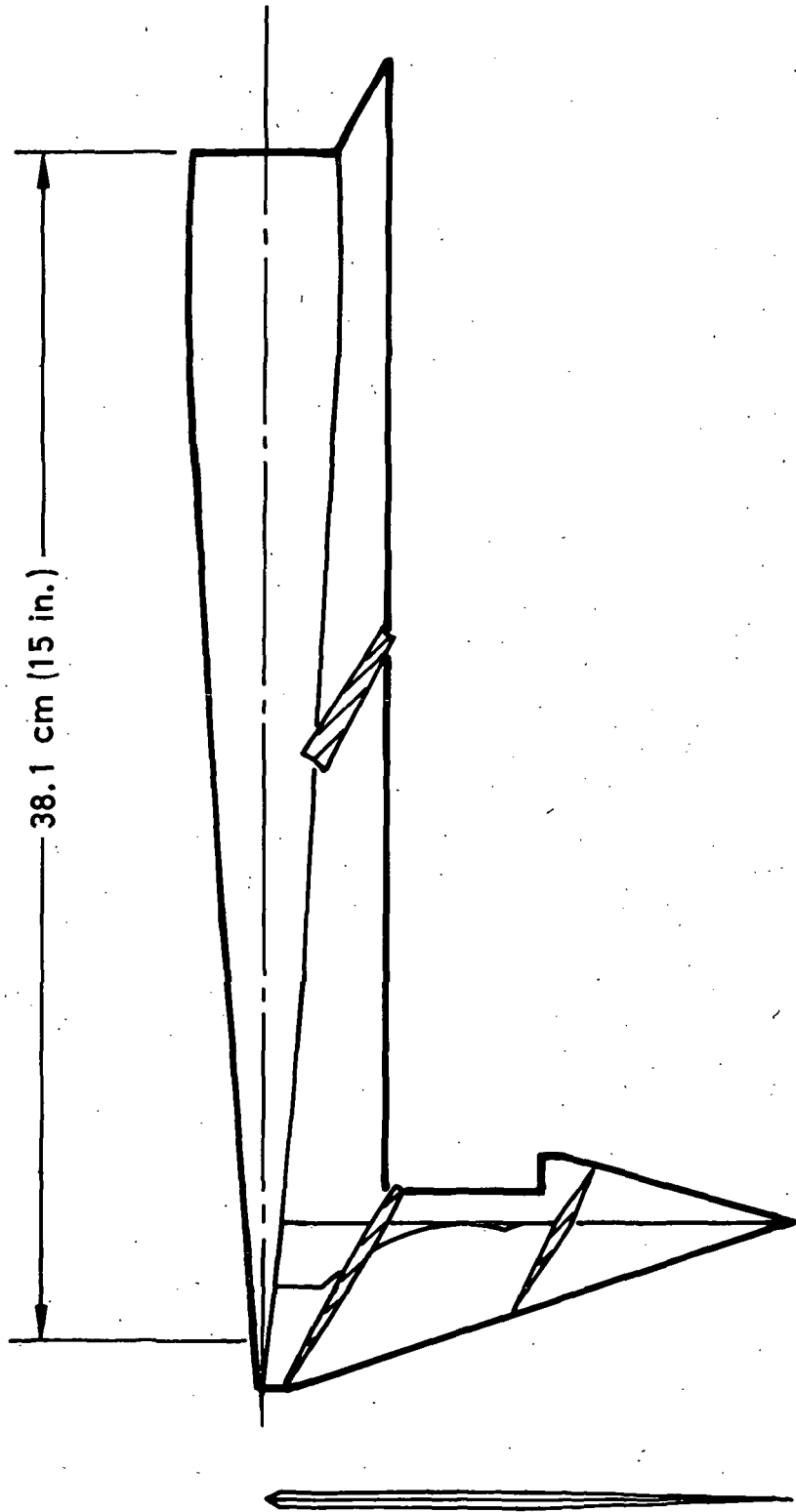


Figure 9. Thermal Fin Model

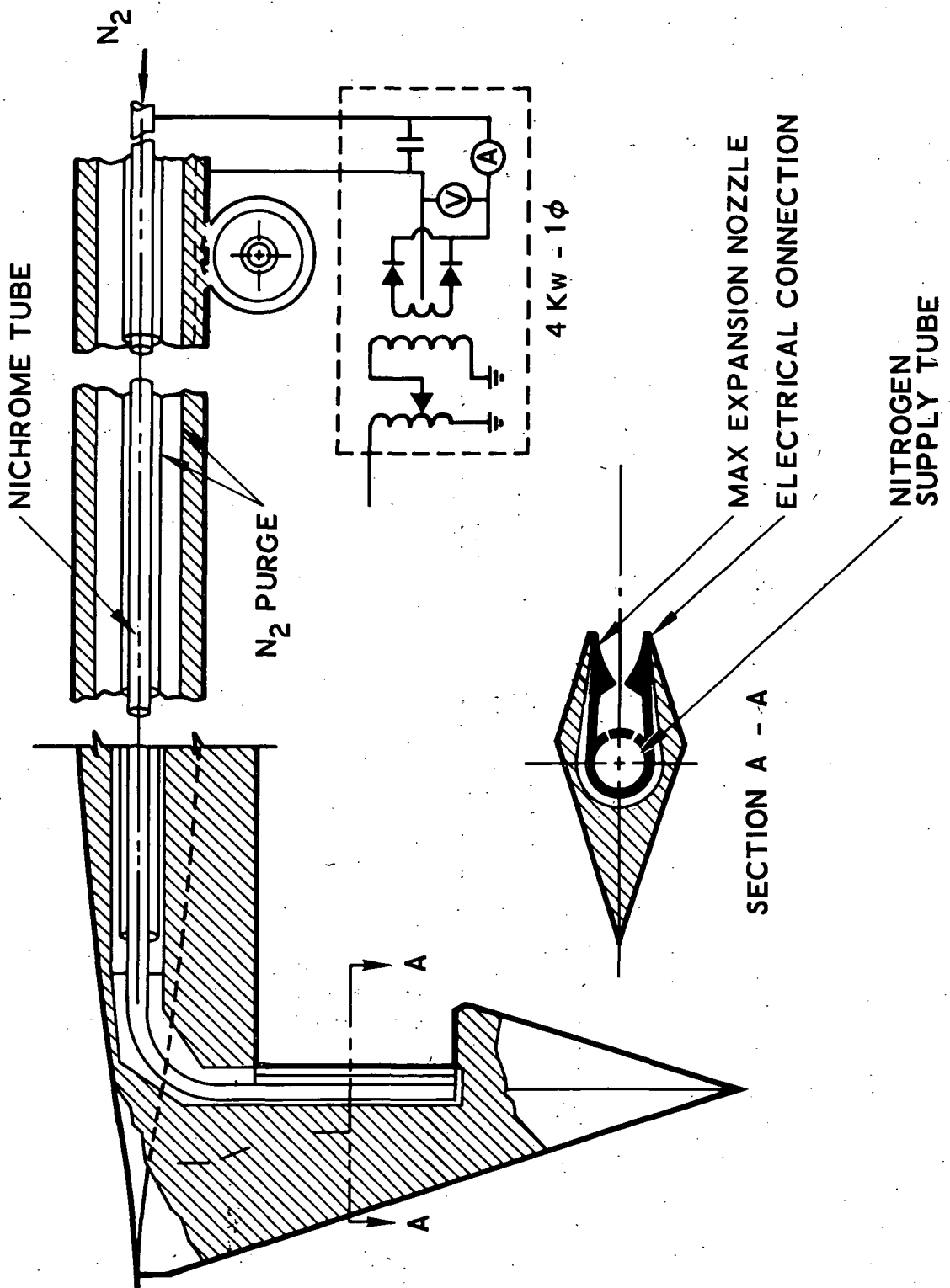


Figure 10. Thermal-Fin Model Cross Section

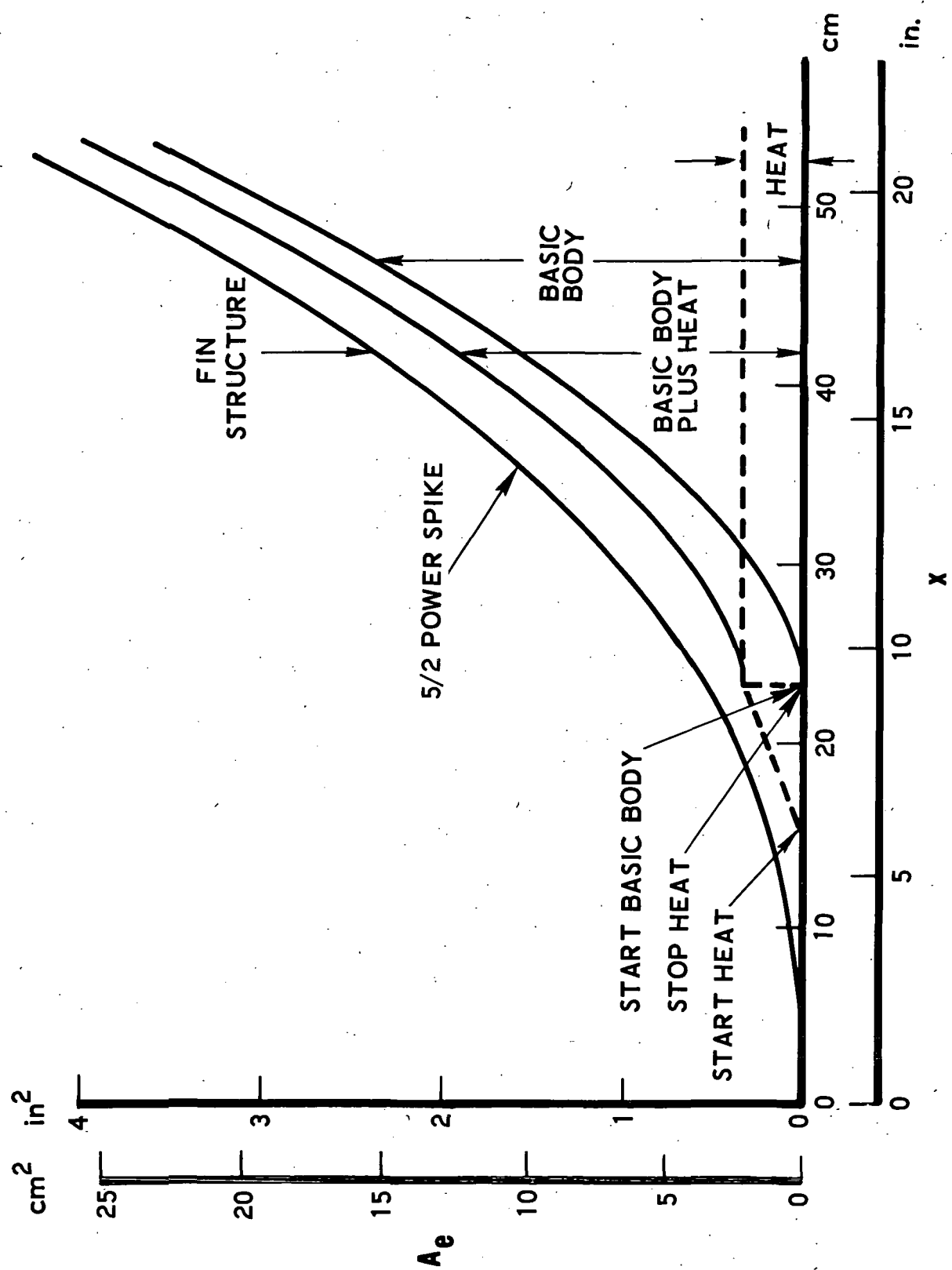


Figure 11. Thermal-Fin Mach-Plane Area Distribution

The sixth model tested is the so-called wing-body model consisting of a body of revolution and a double delta wing for which the sum of the Mach cutting-plane areas due-to-volume and the equivalent Mach-plane area due-to-wing lift is equal to the Mach-plane area distribution of the basic body of revolution (fig. 12). Then, according to linearized theory and the basic sonic-boom signature theory of Whitham, this model should have a pressure signature below it in the lateral symmetry plane through the fuselage centerline equal to that of the basic body.

The wing is a 67.5-degree sweep-angle double delta set at 40 minutes angle of attack. The lift for the wing was calculated using the theory of Polhamus (ref. 18); details are given in Appendix A. At the end of the body, the equivalent area due-to-lift represents about 30 percent of the total effective area.

The seventh model tested is the wing-body model with the solid fin of Model 3 attached below it. The purpose of this model was to test the effectiveness of the fin in generating a finite rise-time signature in the presence of a lateral lift distribution.

3. RESULTS AND DISCUSSION

The results for the measured pressure signatures are shown in figures 13-29. In these figures, the nondimensionalized overpressure $\Delta p/p_\infty$ is shown as a function of distance, $x - \beta r$, behind the Mach line through the point of initial model disturbance at a fixed perpendicular distance r from the centerline of the body (fig. 2). Signatures were taken at values of $r = 50.8$ cm and 76.2 cm (20 in. and 30 in.) for all except the thermal-fin model, corresponding, respectively, to two and three body lengths for the nominal ten-inch models. For the 38.1-cm (15-in.) thermal-fin model, signatures were taken at $r = 76.2$ cm (30 in.), corresponding to two body lengths. Thus, all signatures are of the near field.

Figures 13 and 14 show the results for the basic body-of-revolution airplane. Comparison is shown with theoretical predictions made using a computer code developed at NASA-Langley (ref. 13) based on the theory of Whitham (ref. 17). Note that, in general, the agreement with theory is good. The magnitude of the front shock overpressure and rear expansion are underpredicted, however, and the positions of the rear expansion and rear shock are somewhat in error. A possible explanation for the latter is the fact that the theory assumes that all disturbances originate on the body axis rather than on the body surface, which would cause the theoretical disturbance to be displaced downstream.

Figures 15 and 16 show a comparison of theoretical and experimental pressure signatures for the frontal spike model. Note the excellent agreement with theory in this case, the measured data very nearly following the predicted linear pressure rise.

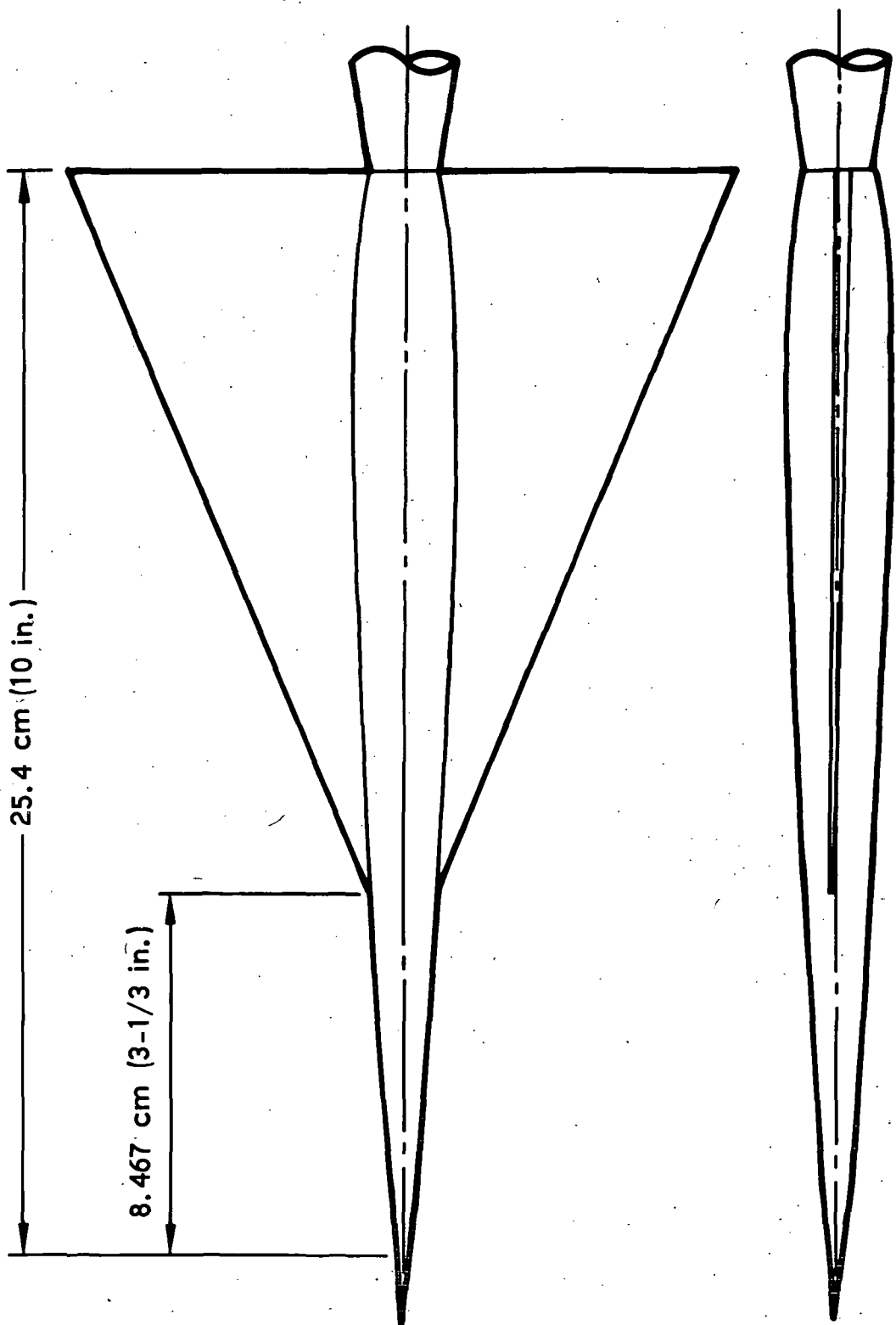


Figure 12. Wing-Body Model

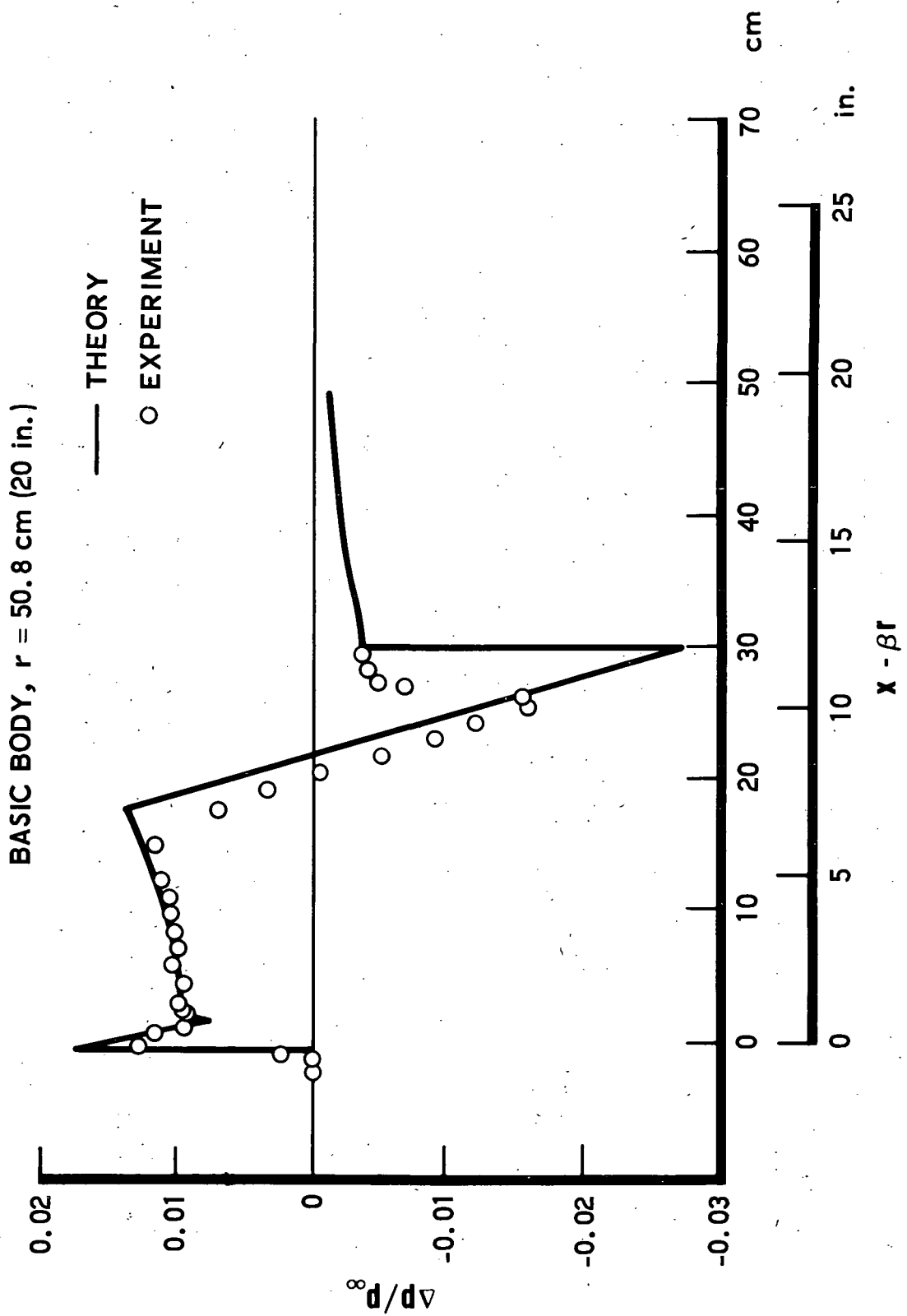


Figure 13. Comparison of Experimental and Theoretical Pressure Distributions

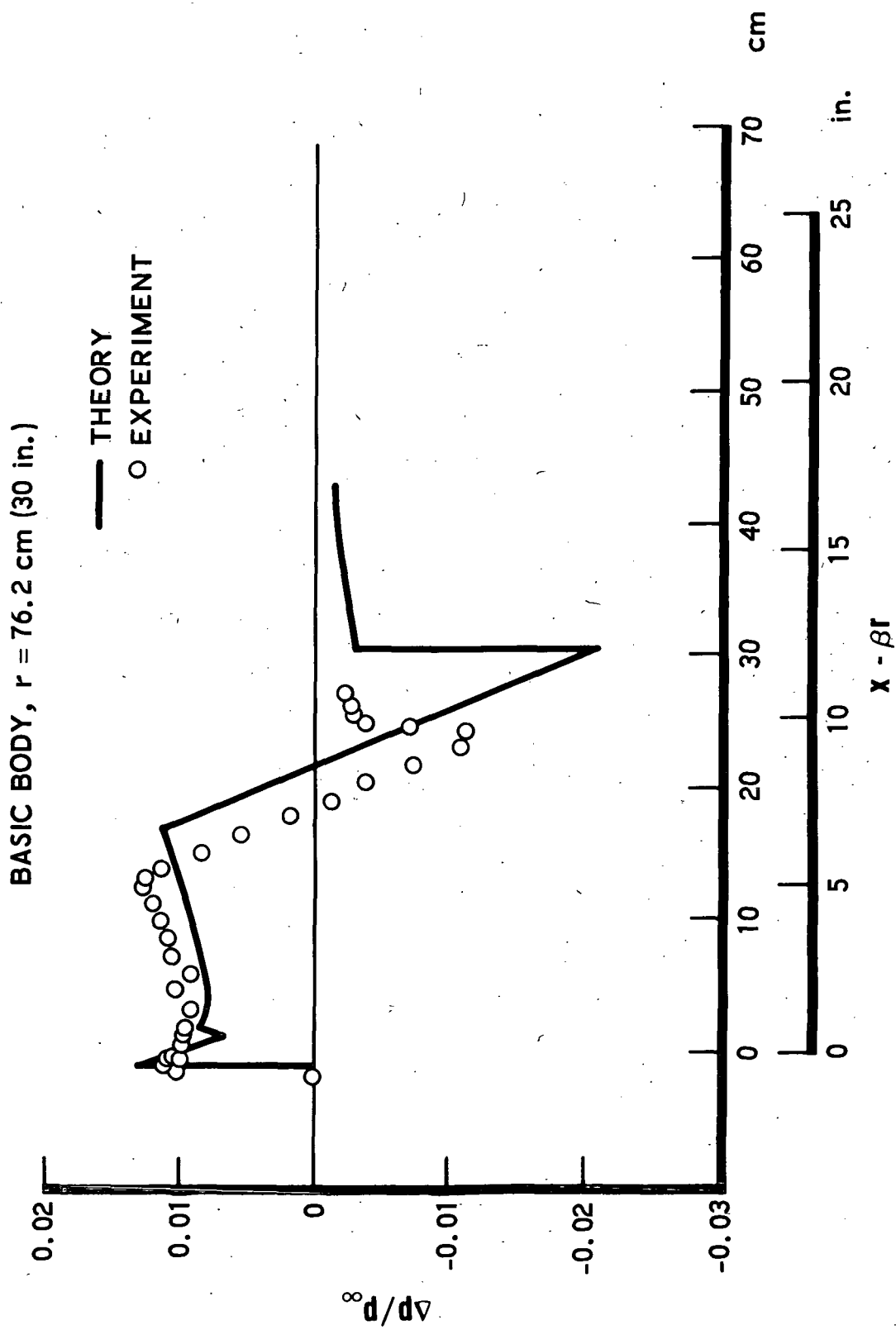


Figure 14. Comparison of Experimental and Theoretical Pressure Distributions

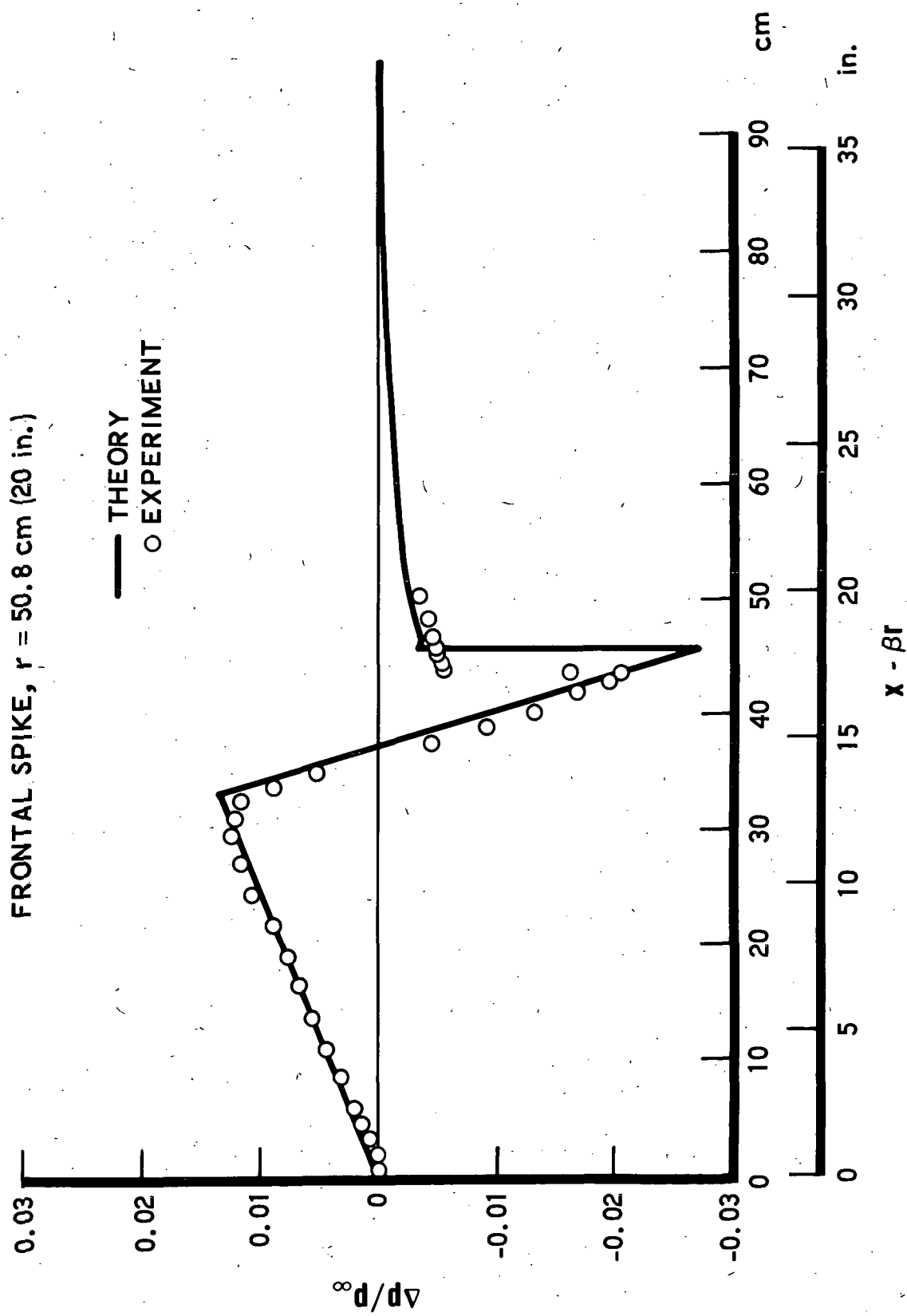


Figure 15. Comparison of Experimental and Theoretical Pressure Distributions

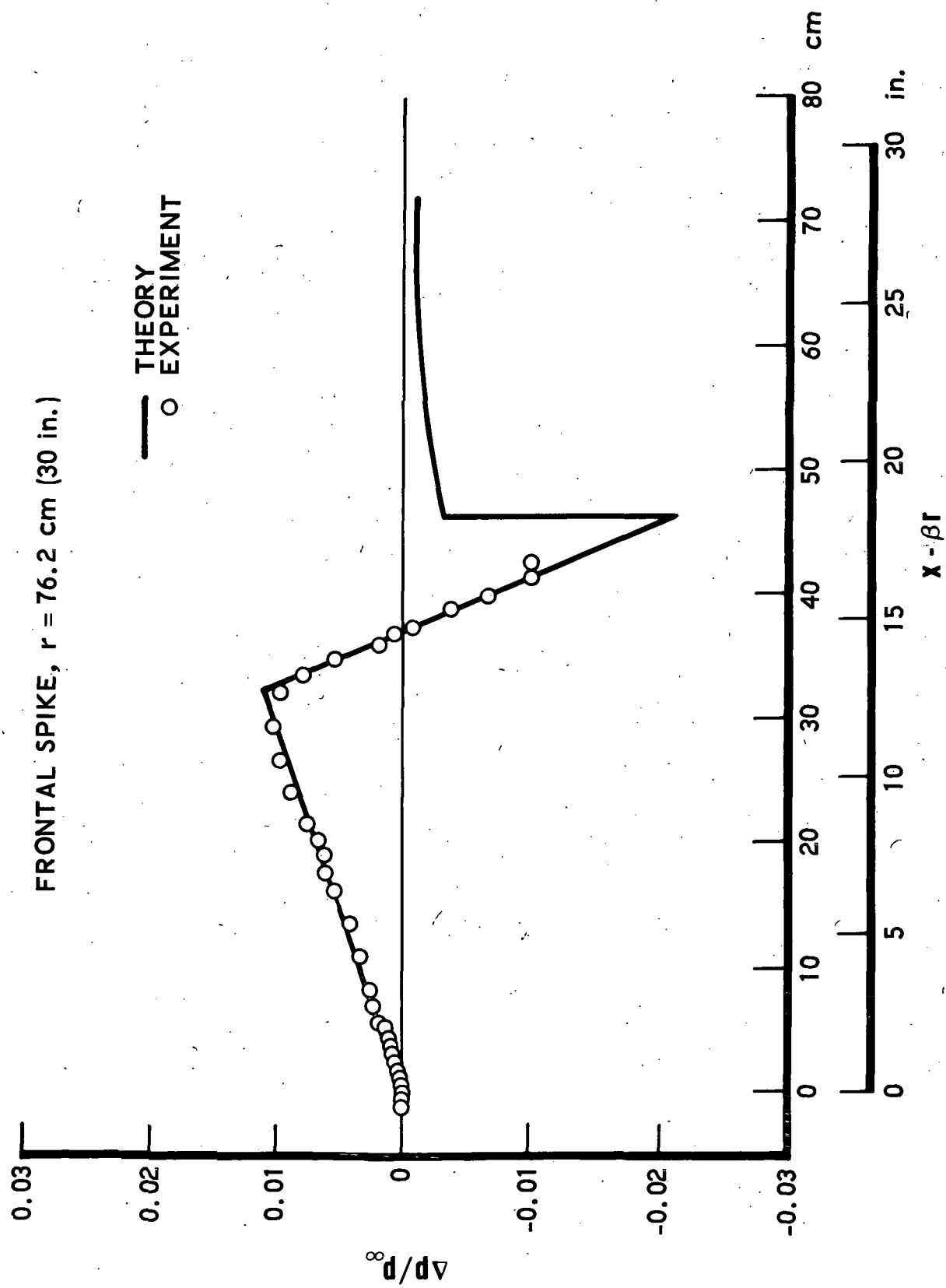


Figure 16. Comparison of Experimental and Theoretical Pressure Distributions

The most important data, of course, are those generated by the solid fin, the twin-body, and the thermal-fin models. The results for the solid fin are shown in figures 17 and 18. Recall that the fin is area-ruled such that the area distribution in Mach cutting planes is identical to that of the 5/2-power frontal spike. In addition, the fin is designed such that disturbances to the free stream are small. When these two conditions are met, a pressure signature in the plane of symmetry below the fin identical to that of the 5/2-power spike is predicted. Note that such a result is nearly obtained in figures 17 and 18. The important question, of course, is whether any local compression regions will cause a shock wave to develop at larger distances. Two such regions are seen at $r = 50.8$ cm (20 in.) in figure 17, one at the beginning and one toward the end of the linear pressure-rise region. When the signature at $r = 76.2$ cm (30 in.) in figure 18 is considered, however, it is seen that no significant steepening has occurred for the compressive region at the beginning, and the one toward the end of the linear region has nearly disappeared. Even if shock waves developed from these compressions, however, they would be no more than ten percent of the total pressure rise.

The results for the twin-body model were not as encouraging, however. These are shown in figures 19, 20, 21 and 22. Figures 19, 20 and 21 give the signatures at $r = 50.8$ cm (20 in.) for a separation distance, S , of 8.89 cm (3.5 in.) and various settings of relative lengths, L (see fig. 8 for definitions of S and L). The L_0 corresponds to the nominal setting as would be predicted by linearized theory, i.e., all Mach lines at their undisturbed free-stream positions. Figure 19 shows a local steep compression occurring about 15 cm into the signature, followed by an overexpansion and subsequent recompression. This is caused by the disturbance coming off of the nose of the basic-body of the twin-body model, the signature up to that point being due only to the lower body. Recall that the basic body was designed with a local 5/2-power cusped nose 1.359 cm (0.535 in.) in length such that a shock would not form prior to a radial distance, r , of about 25 cm (Appendix A). Expansions from the shoulder of the lower body are designed to interact and partially cancel the compressions originating from the cusped nose, thereby maintaining the linear growth. Since the Mach number of the tunnel flow is in actuality slightly above two (2.01), the first relative-length setting, L , was made at a value 0.1588 cm (0.0625 in.) less than nominal to account for this. An initial compression was noted (fig. 19) and it was thought that perhaps the expansions from the lower body were not coming into play soon enough. To correct for this, a second run was made with a value of $L = 0.635$ cm (0.25 in.) ahead of nominal (fig. 20). Note that the initial compression is now replaced by an expansion, with a subsequent overcompression and re-expansion. Thus, the lower body has been moved too far forward to provide the desired cancellation. The results of moving it back to a position 0.1588 cm (0.0625 in.) ahead of nominal are shown in figure 21. Even though the initial expansion is nearly eliminated, the strong overcompression is still present. As a matter of fact, comparison of figures 19, 20 and 21 reveals that the peak of the local overpressure region remains at the same position and is of the same magnitude for all three relative body positions, thereby indicating a negligible effect of the lower-body expansion on the compression off of the nose of the upper body. One possible explanation for this is the boundary-layer displacement thickness effect, which tends to enhance the compression and weaken the expansion.

SOLID FIN MODEL, $r = 50.8$ cm (20 in.)

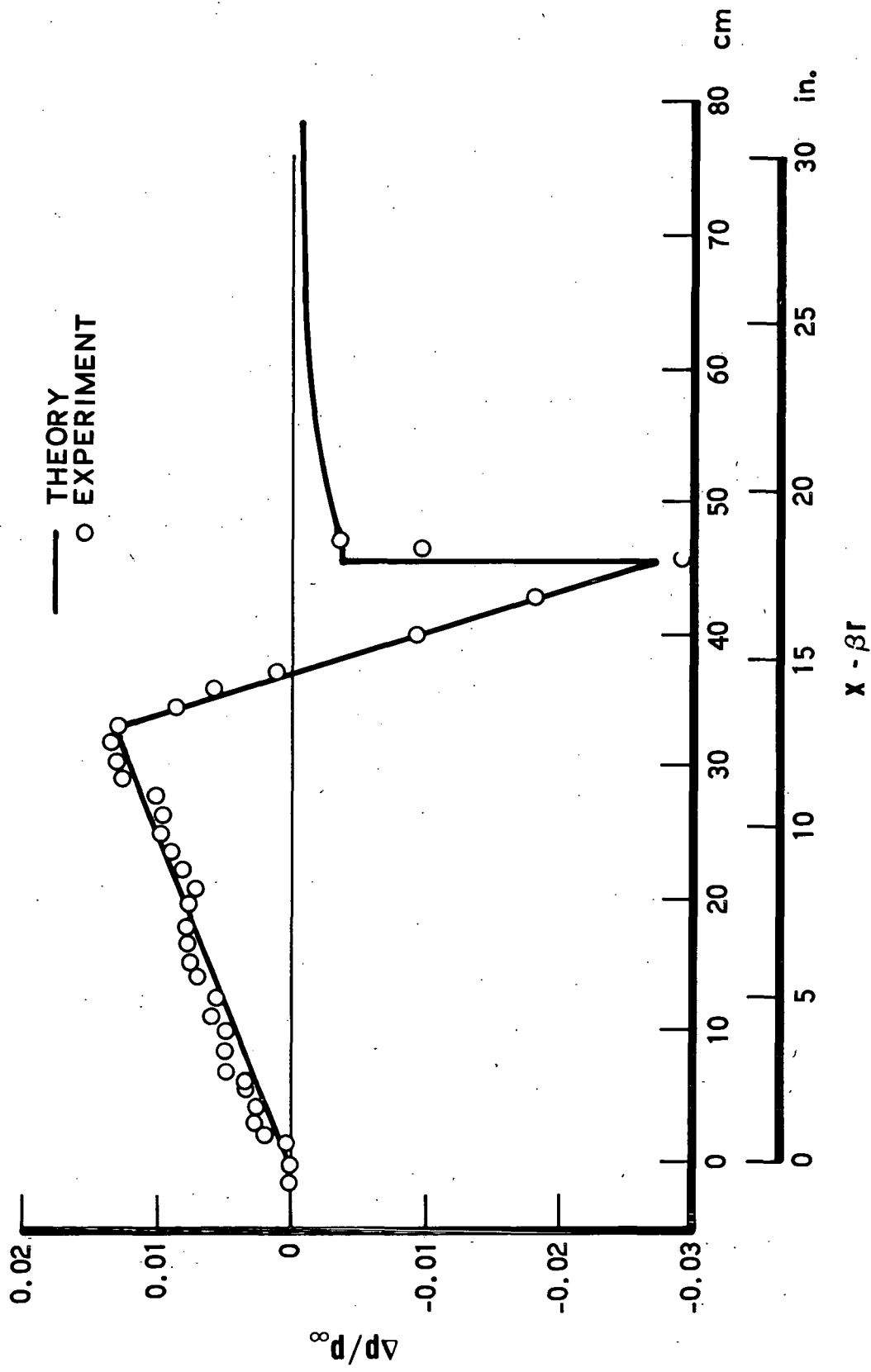


Figure 17. Comparison of Experimental and Theoretical Pressure Distributions

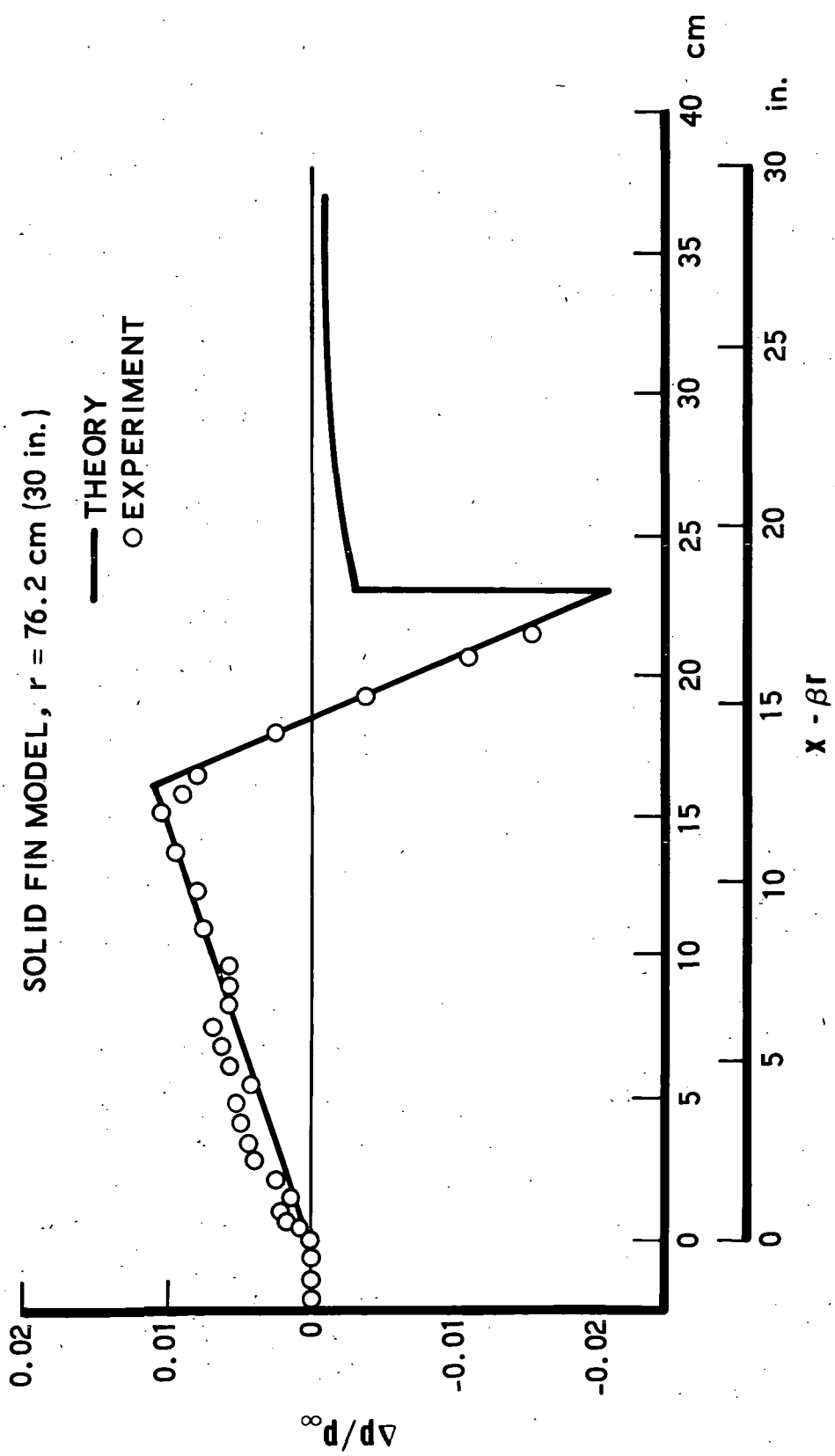


Figure 18. Comparison of Experimental and Theoretical Pressure Distributions

TWIN-BODY MODEL, $S = 8.89 \text{ cm (3.5 in.)}$

$r = 50.8 \text{ cm (20 in.)}, L = L_0 - 0.3175 \text{ cm}$

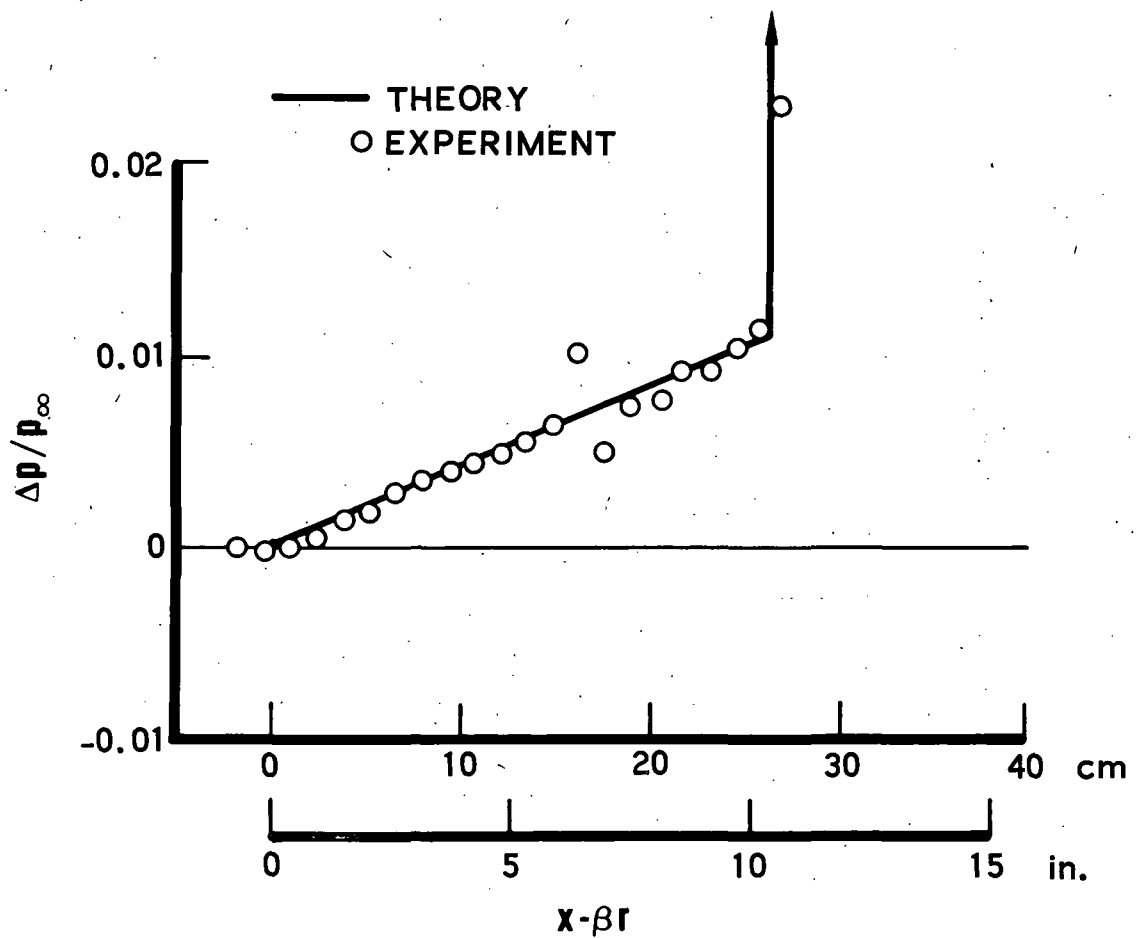


Figure 19. Comparison of Experimental and Theoretical Pressure Distributions

TWIN-BODY MODEL, $S = 8.89 \text{ cm (3.5 in.)}$

$r = 50.8 \text{ cm (20 in.)}, L = L_0 + 0.635 \text{ cm}$

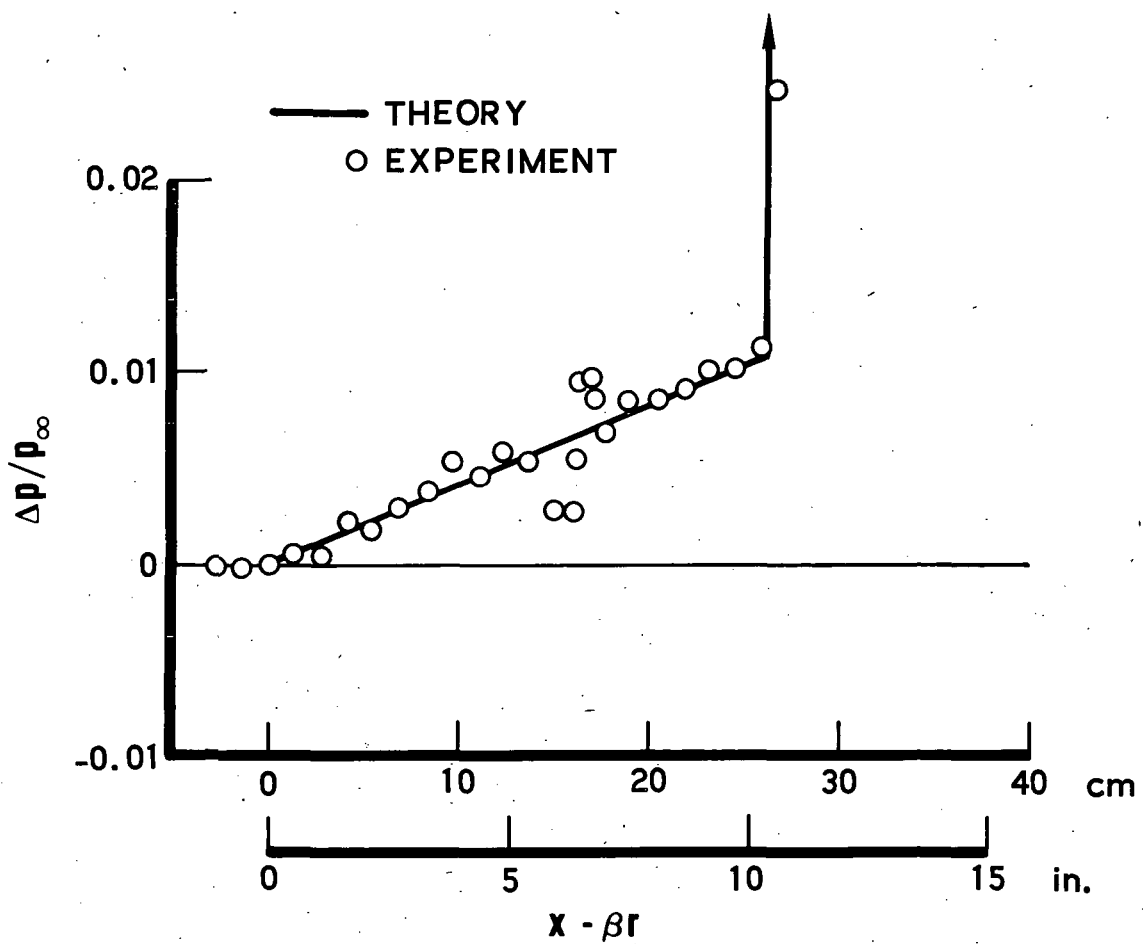


Figure 20. Comparison of Experimental and Theoretical Pressure Distributions

TWIN-BODY MODEL, $S = 8.89$ cm (3.5 in.)
 $r = 50.8$ cm (20 in.), $L = L_0 + 0.3175$ cm

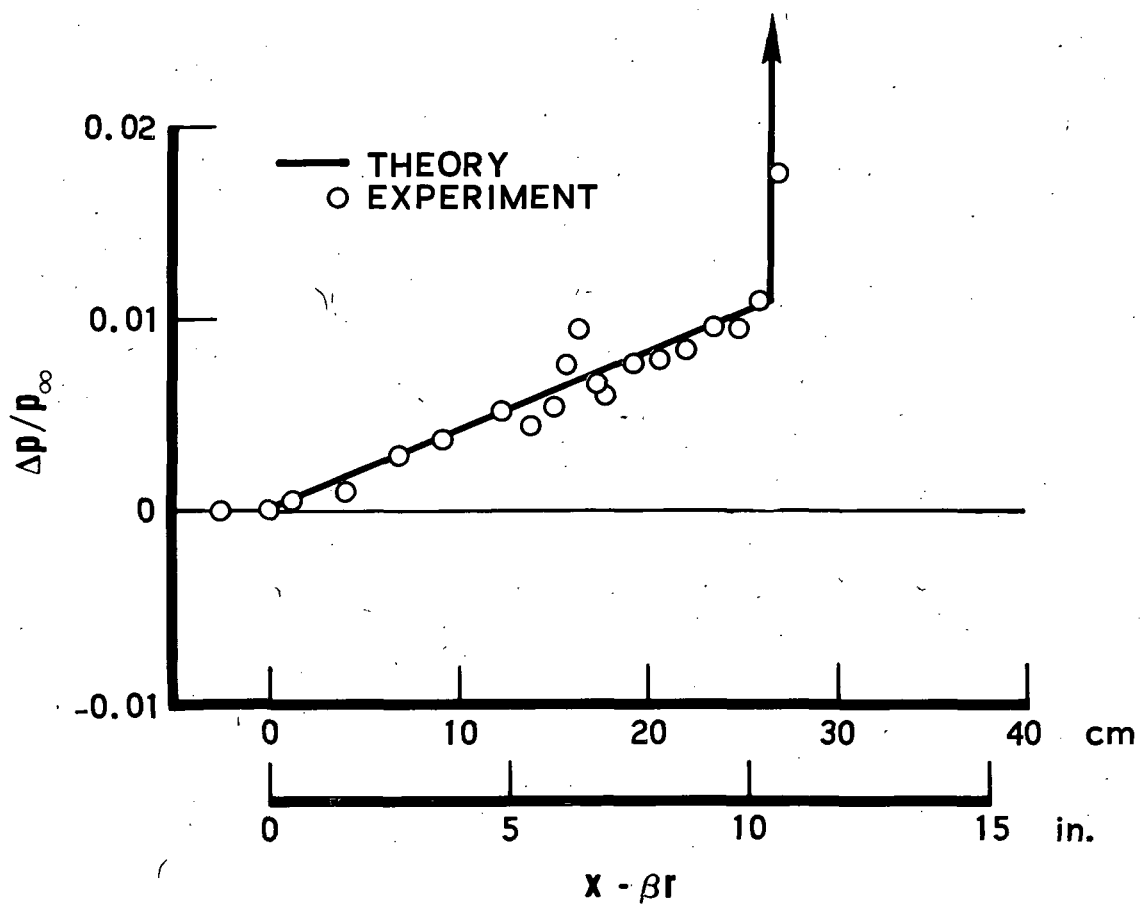


Figure 21. Comparison of Experimental and Theoretical Pressure Distributions

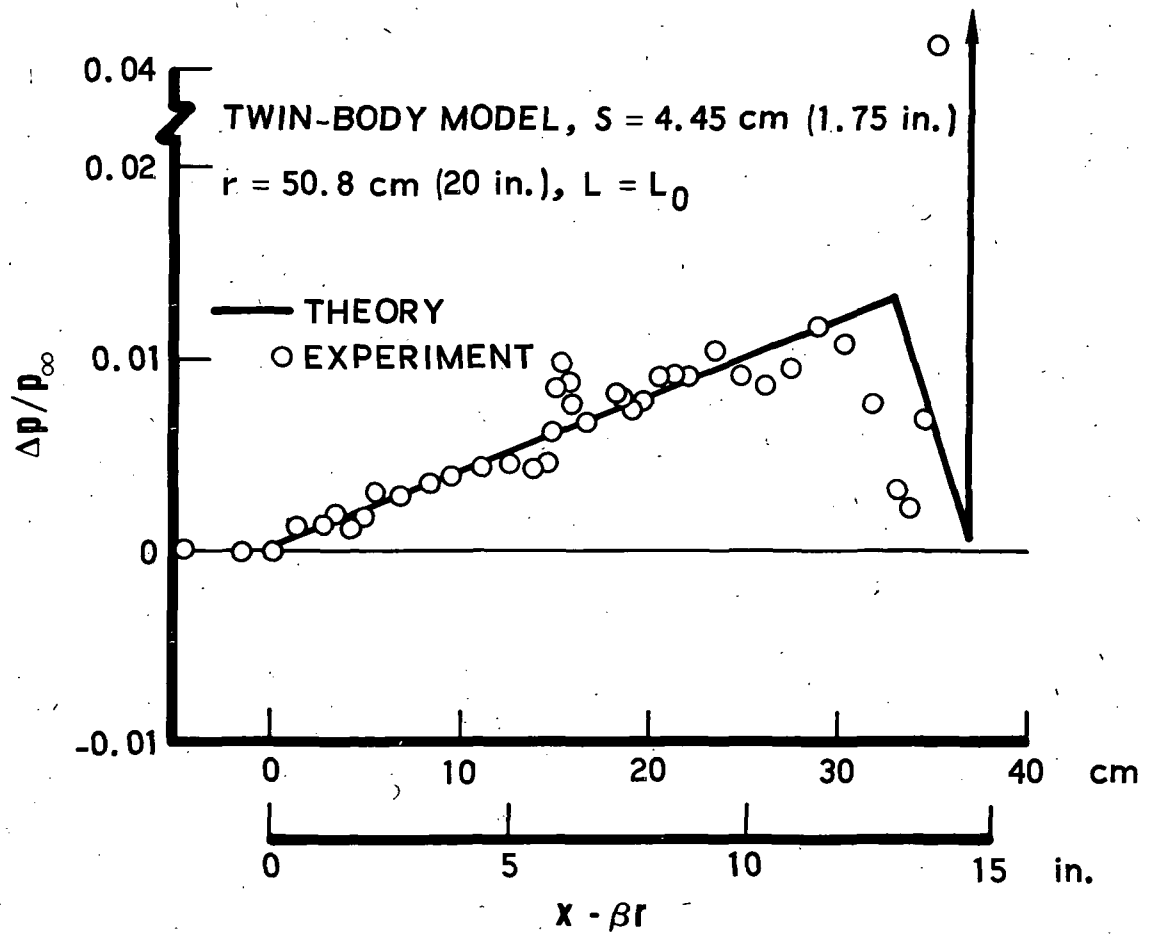


Figure 22. Comparison of Experimental and Theoretical Pressure Distributions

This effect could be investigated by compensating for the boundary-layer displacement thickness in the body contours. The shock wave occurring at about $x - \beta r = 25$ cm is due to the compression generated off of the lower body support (fig. 8).

Similar results to those at the 50.8 cm (20 in.) station for the 8.89 cm (3-1/2 in.) separation were obtained at the 76.2 cm (30 in.) station. In addition, a result for the 4.445 cm (1.75 in.) separation is shown in figure 22 at the nominal relative-length setting. Results similar to those at the 8.89 cm (3.5 in.) separation are noted.

Thus, based on the more favorable results for the solid-fin model than for the twin body, a thermal-fin counterpart was constructed and tested.

The results are shown in figures 23 and 24 for a wind-tunnel total pressure of 51.7 kN/m^2 (7.5 psia) and in figures 25, 26 and 27 for a total pressure of 69 kN/m^2 (10 psia). The former is the design-condition setting to obtain the proper ratio of jet-to-freestream stagnation pressures as determined by the exit static-pressure match condition (Appendix B). Figure 23 shows the resulting signature at $r = 76.2$ cm (30 in.) for the case of no flow through the fin nozzle. Note the large expansion and subsequent recompression. This portion of the signature corresponds to disturbances generated by the nozzle region of the fin, the expansion being generated by the growing area deficit through the nozzle region, and the recompression caused by this deficit becoming constant at the end of that region. Figure 24 shows the result of passing heated nitrogen through the fin at the design mass-flow rate and temperature (Appendices B and C). Note the substantial reduction in the nozzle deficit region, although an expansion still exists at the outset. Visual examination of the model after the test indicated a greater nozzle width in the center than at the ends when the flow was turned on, giving a mass (and hence area) deficit in the lower region of the fin. This is the probable cause of the expansion-recompression region noted in the signature. Further, note the two points marked "cold flow" and "no flow." These were obtained by first turning the heater power off and then turning the nozzle flow off. In this manner, the effects of the flow and heat are separated, and it is seen that they both contribute about equally to the overpressure at this point.

Figures 25, 26 and 27 show the effects of cold and hot flow on the thermal fin pressure signature for a wind-tunnel total pressure of 69 kN/m^2 (10 psia). Although the nozzle is underexpanded at this pressure and the effective-area contribution is only about three-quarters that of the fully-expanded case, note that the effects on the pressure signature are still substantial.

The final models tested were the wing-body and wing-body with solid fin. The objective of these tests was to assess the effectiveness of the solid fin in producing a finite rise-time signature when lift is present in actuality as opposed to its equivalent area form as in the basic body of revolution. Figure 28 shows the results for the wing-body alone compared with the theoretical prediction for the basic body of revolution. Recall that the wing-body was designed so that the sum of the areas due to volume of the fuselage and wing plus the equivalent area due-to-lift of the wing is equal to the area of the

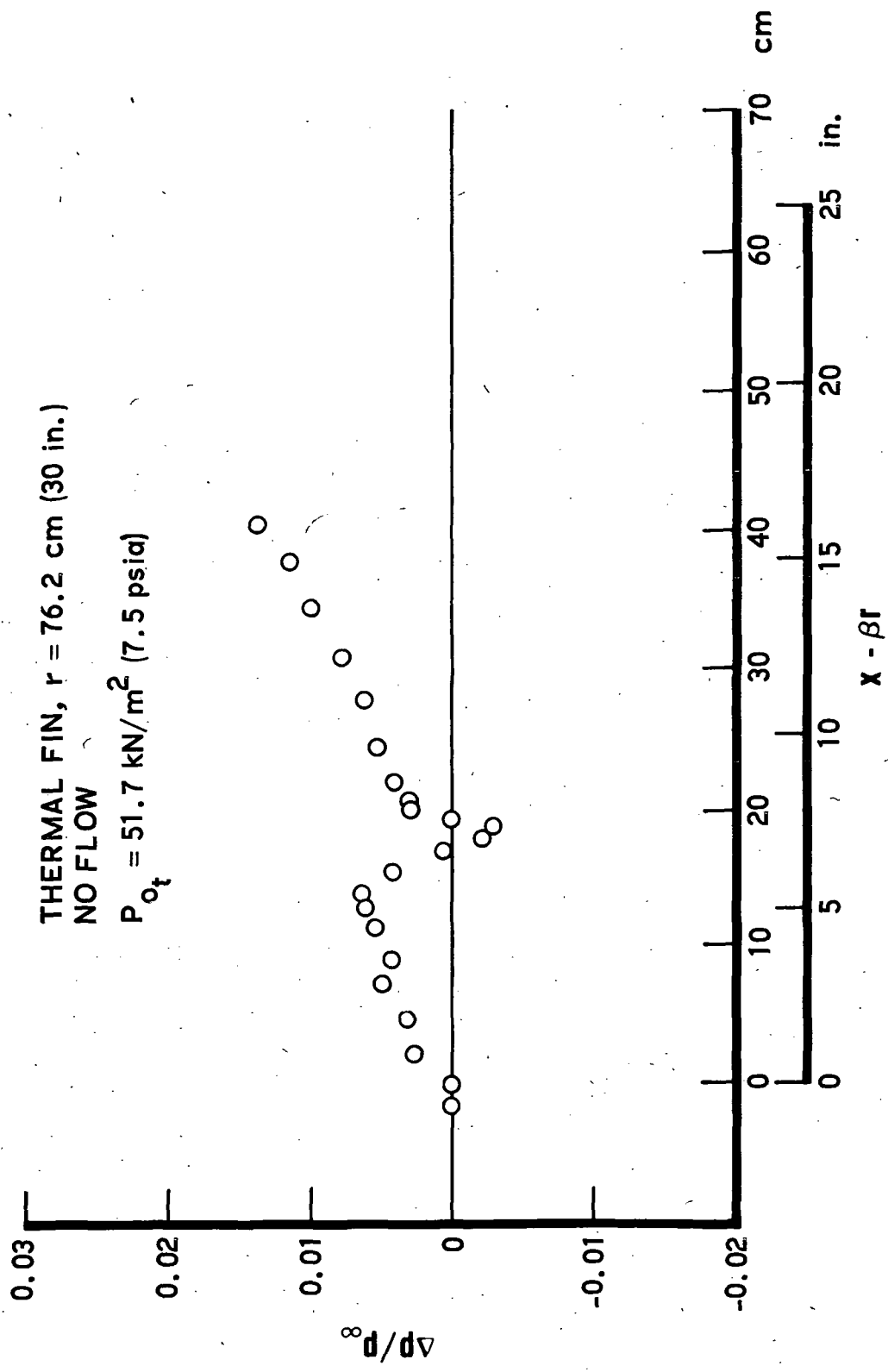


Figure 23. Experimental Pressure Distributions

THERMAL FIN, $r = 76.2$ cm (30 in.)

DESIGN MASS FLOW AND HEAT ADDITION

$$P_{ot} = 51.7 \text{ kN/m}^2 (7.5 \text{ psia})$$

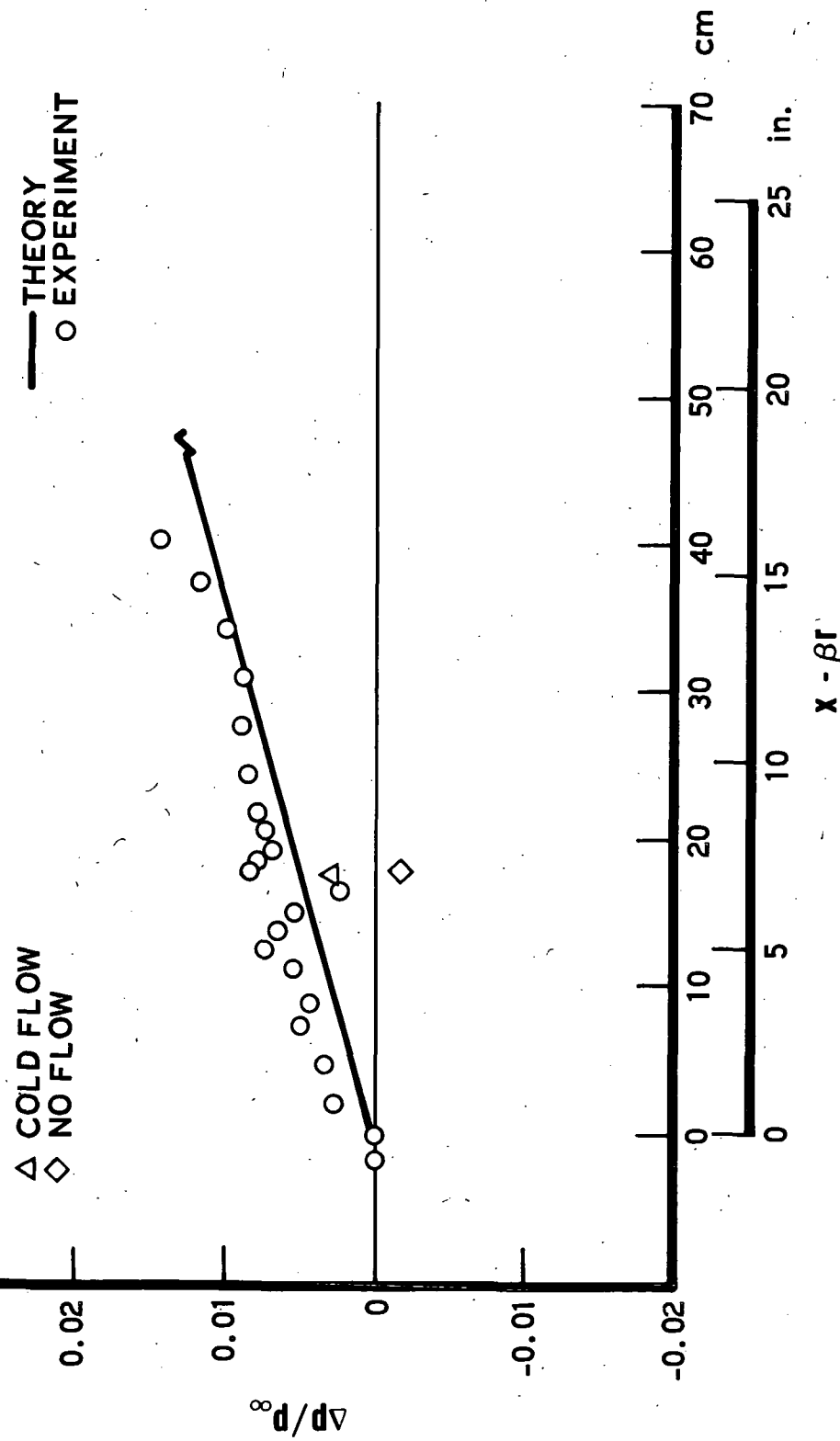


Figure 24. Comparison of Experimental and Theoretical Pressure Distributions

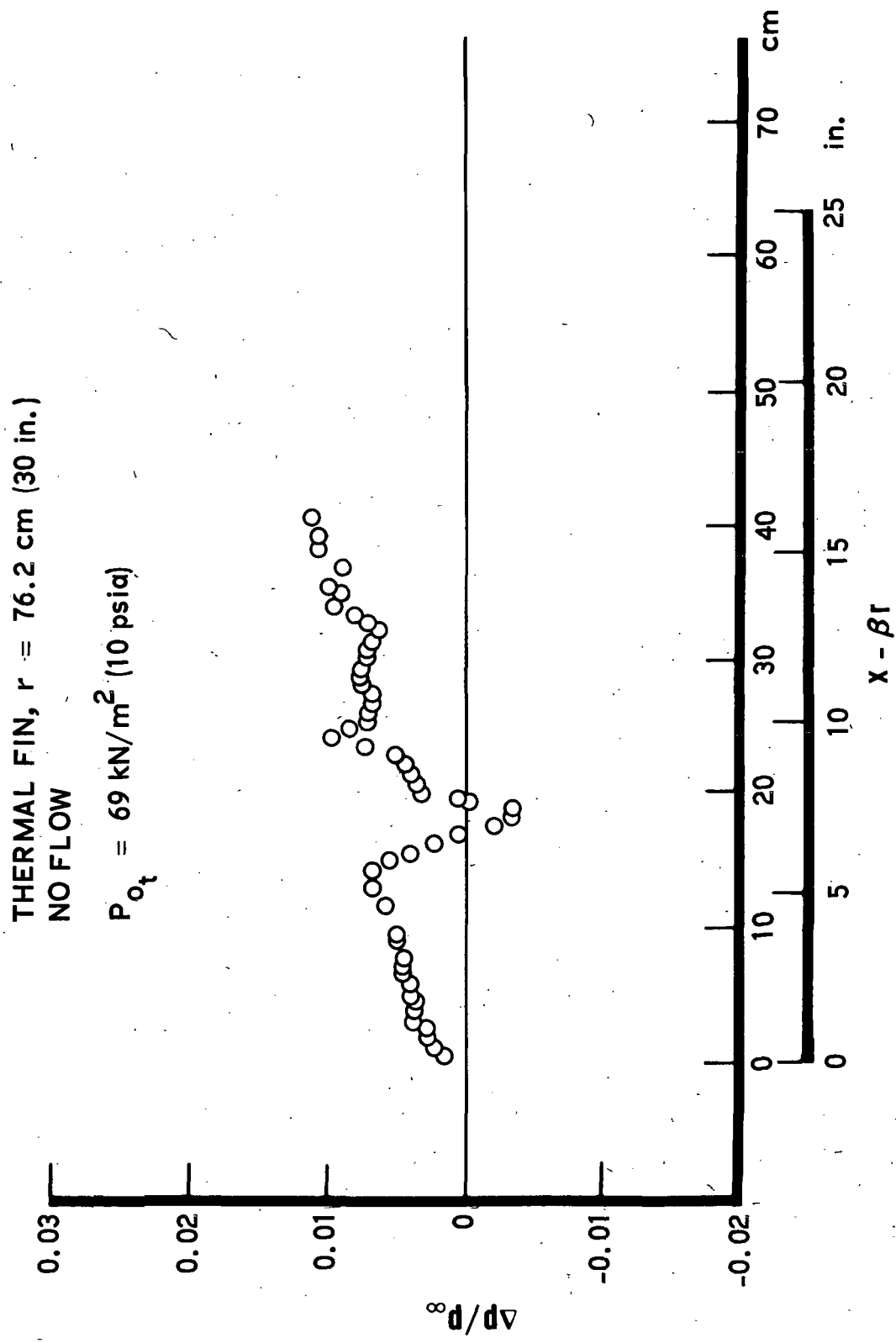


Figure 25. Experimental Pressure Distribution

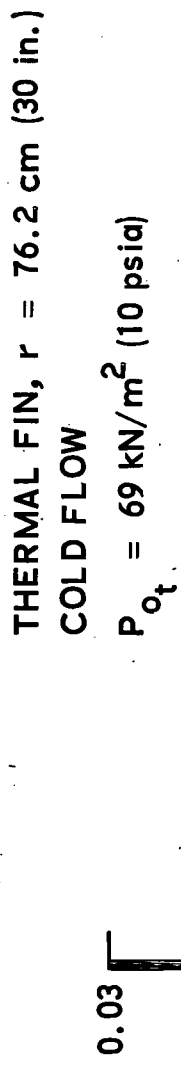


Figure 26. Comparison of Experimental and Theoretical Pressure Distributions

THERMAL FIN, $r = 76.2$ cm (30 in.)
DESIGN MASS FLOW AND HEAT ADDITION
 $P_{ot} = 69 \text{ kN/m}^2$ (10 psia)

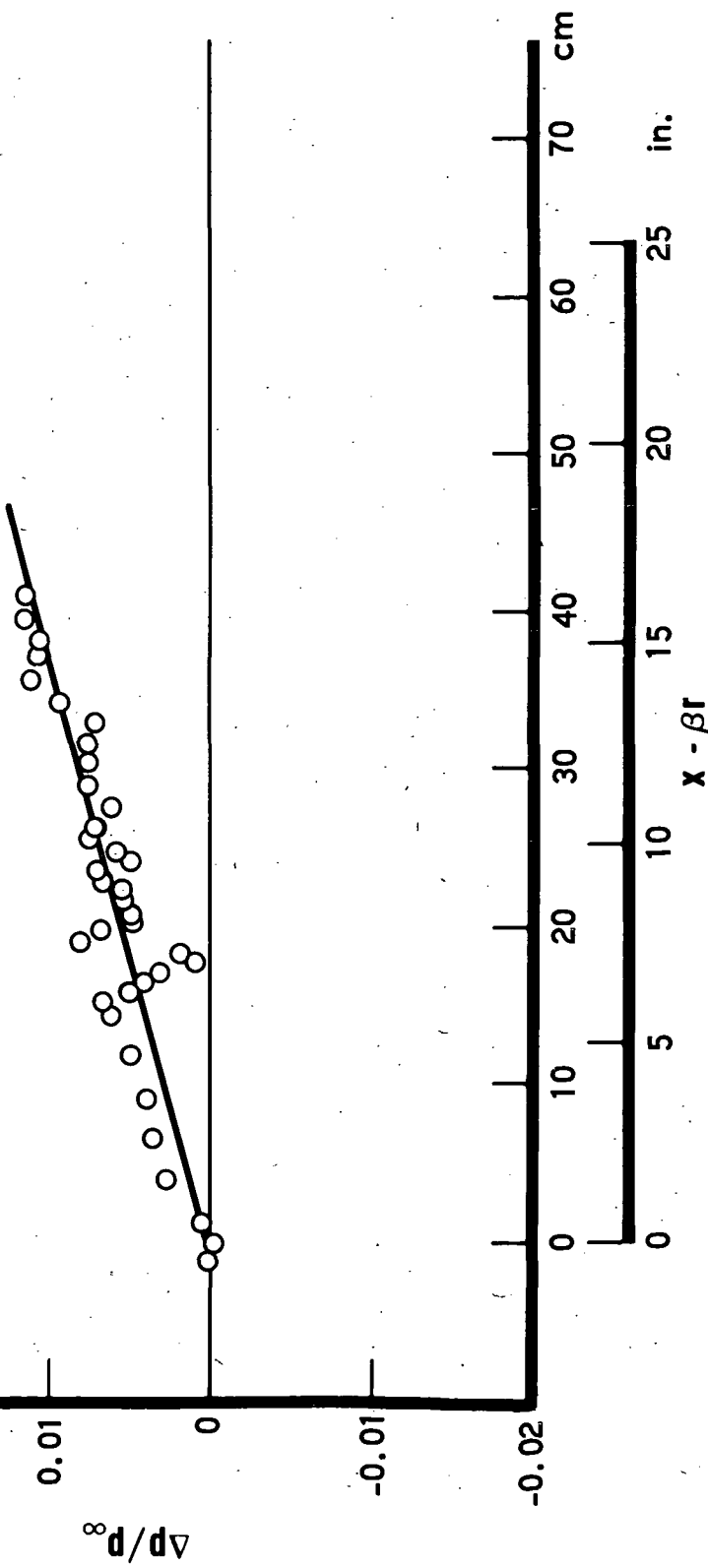


Figure 27. Comparison of Experimental and Theoretical Pressure Distributions

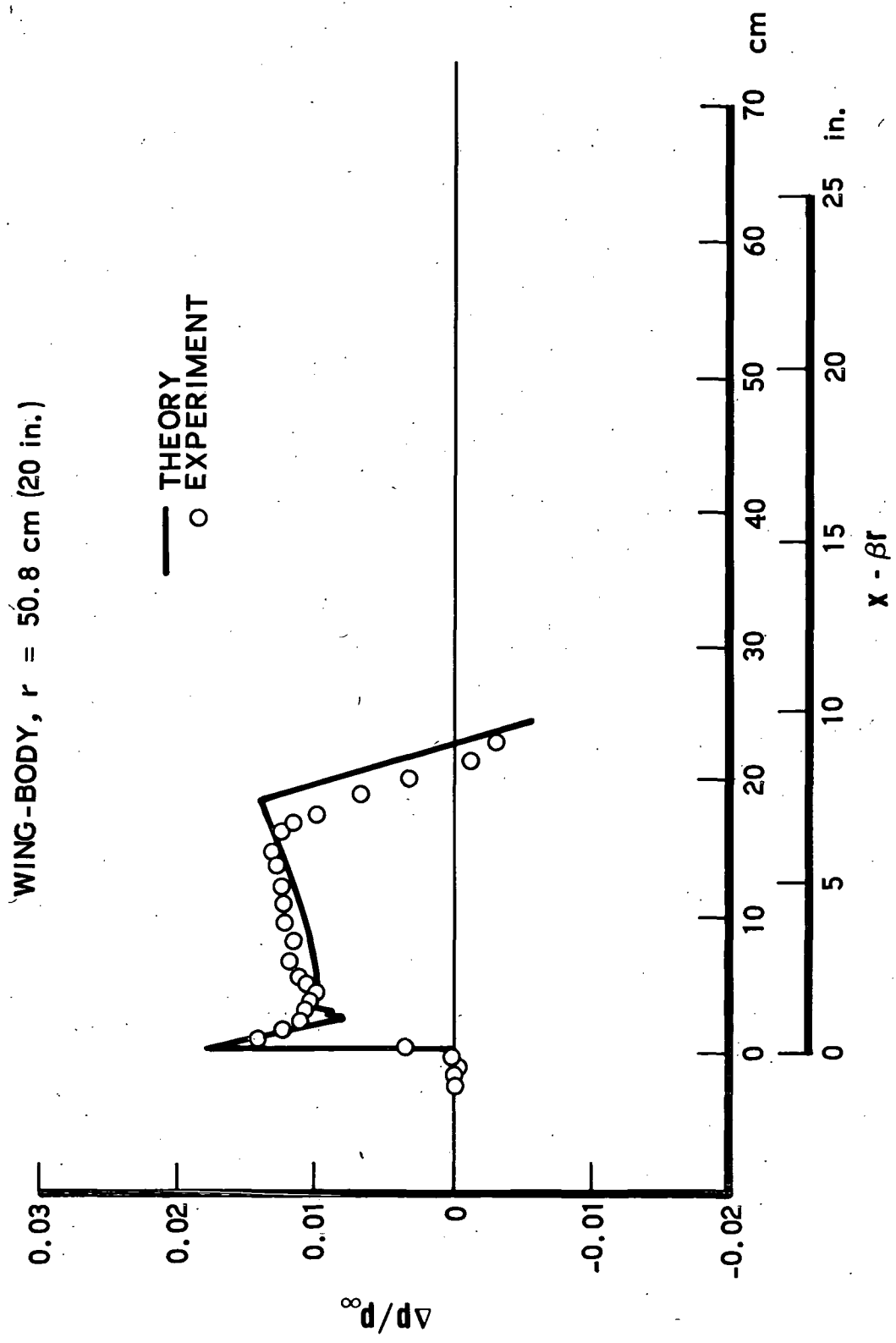


Figure 28. Comparison of Experimental and Theoretical Pressure Distributions

basic body of revolution in each Mach plane. Hence, the wing-body should have the same pressure signature as the basic body of revolution. The experimental results of figure 27 compare well with the theoretical prediction for the basic body and with the experimental results of figure 11, thereby verifying the equivalence.

Figure 29 shows the results of adding the solid fin previously tested in conjunction with the basic body of revolution (fig. 5) to the wing-body model. The resulting pressure signature compares well with the theoretical prediction except in a small region where the nose of the basic body begins to affect the signature. A sudden expansion followed by a gradual recompression is noted in this region. One probable cause of this is a small gap between the fin and basic body in that region that was noted upon detailed examination of the model after the test data were taken.

4. CONCLUSIONS

Based on the results of the wind-tunnel tests reported herein, several conclusions may be drawn. Most importantly, the use of heat fields to provide effective areas through streamtube expansion has been verified. In addition, it has been shown that off-axis structures and/or heat fields may be used to produce finite rise-time sonic-boom signatures. Moreover, such structures are effective in producing a finite rise-time signature in the ground track in the presence of a lateral lift distribution.

5. SUGGESTED FUTURE RESEARCH

Major criticism of the heat-field approach to sonic-boom alleviation has centered upon two areas; first, the lack of this approach to significantly reduce acoustic energy in those frequencies to which structures respond, and second the large penalties associated with means of implementing this approach into a practical aircraft design.

The indoor noise characteristics are mainly a function of signature impulse and overpressure. Since the area distribution for minimum overpressure varies with distance from the aircraft nose to the $3/2$ power whereas that for finite rise time has a $5/2$ -power variation, it is not possible to achieve a minimum overpressure finite rise-time signature. Hence, the best that can be done in answer to the first criticism above is to minimize the peak overpressure increase associated with implementation penalties to obtain a finite rise-time signature. Cursory studies of these penalties have been undertaken by several investigators (refs. 1, 8, 9). A design study of an aircraft taking into account the capability of producing a finite rise-time signature as an integral part of the design has not been performed, however. Such a study would be in order to properly assess and minimize the penalties associated with achievement of a finite rise-time signature.

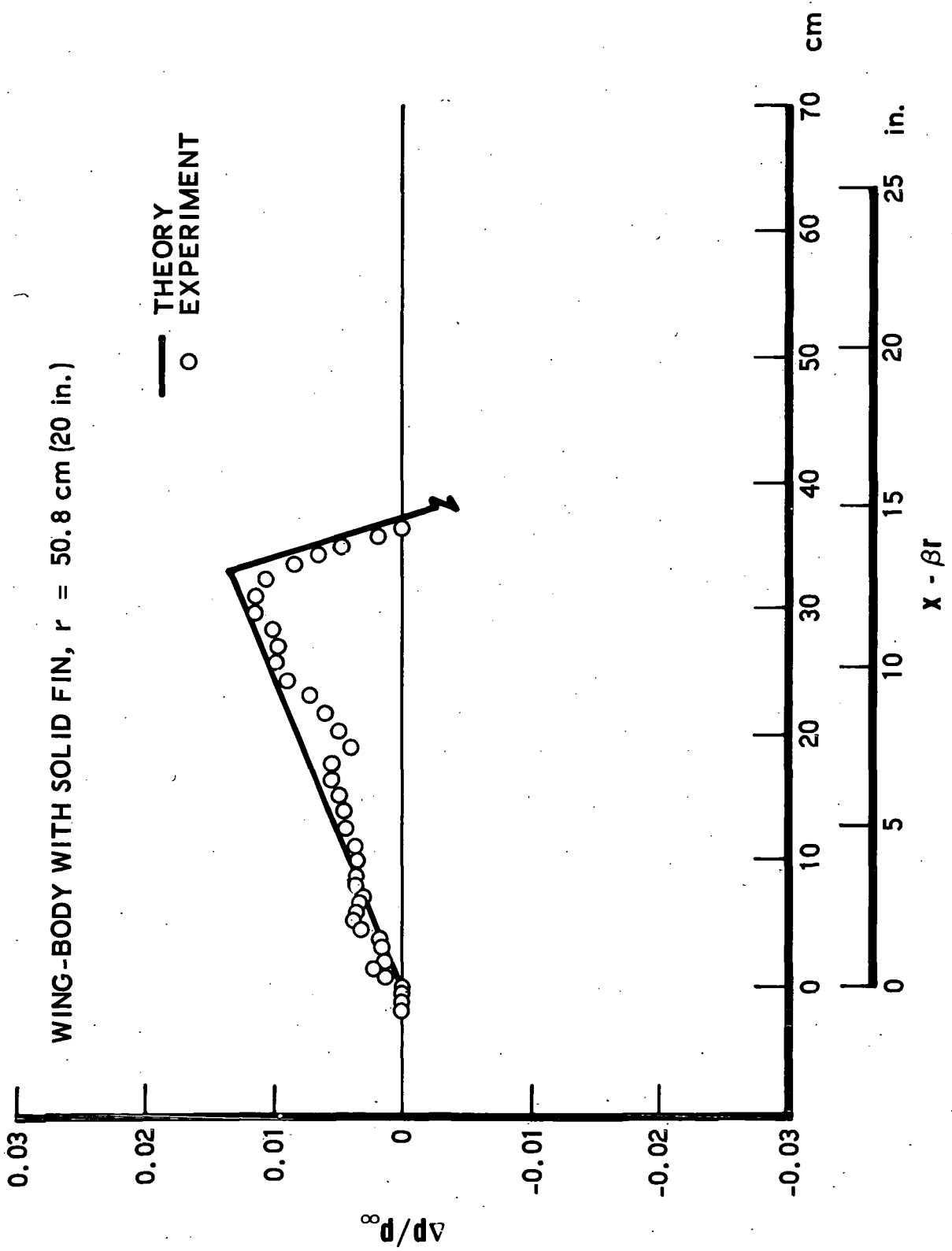


Figure 29. Comparison of Experimental and Theoretical Pressure Distributions

APPENDIX A

DESIGN EQUATIONS FOR BASIC BODY, FRONTAL SPIKE, SOLID FIN, THERMAL FIN, AND WING-BODY MODELS

A. 1 Basic Body of Revolution and Frontal Spike

The basic body of revolution and 5/2-power frontal spike models were designed in conjunction with one another to satisfy the requirement that if the 5/2-power frontal spike were simulated by a heat field, the front shock would be eliminated by heat addition only, with the heating ending at the nose of the basic body. In addition, in order to obtain a finite rise-time signature on the ground in the equivalent full-scale sense for a 272,155-kg (600,000-lb) aircraft flying at 18,288-m (60,000-ft) altitude, it was desired that the frontal spike begin 60.96 m (200 ft) in front of the basic body (fig. 6). Considering the representative SST area distribution of fig. 4, the 5/2-power contour is maintained up until $x = 68.58$ m (225 ft). Thus, two equations for the 5/2-power constant of proportionality and heated area increment are provided. The remaining contour from 68.58 m (225 ft) to 91.44 m (300 ft) was fit with a cubic equation. There results, for the model frontal spike area distribution to a scale of 1 cm = 3.6 m (1 in. = 30 ft):

$$-16.93 \text{ cm} \leq x \leq 19.05 \text{ cm } (-20/3 \text{ in.} \leq x \leq 15/2 \text{ in.}):$$

$$A_S = 0.946 \times 10^{-3} (x + 16.93)^{5/2} \text{ cm}^2$$

$$19.05 \text{ cm} \leq x \leq 25.4 \text{ cm } (15/2 \text{ in.} \leq x \leq 10 \text{ in.}):$$

$$A_S = -0.567 \times 10^{-2} (x + 16.93)^3 + 0.591(x + 16.93)^2 \\ - 19.975(x + 16.93) + 225.47 \text{ cm}^2$$

A 5/2-power cusp was fitted to the nose of the basic body to prevent a shock from forming in front of the fin when used with the fin attached (see below). To prevent shock formation before a nominal distance of 25.4 cm (10 in.) below the model, it is required that the advance be such that $x - \beta r = 0$ at $r = 25.4$ cm, i.e., from the theory of Whitham (ref. 17), the characteristics are given by

$$y = x - \beta r + kF(y)r^{1/2}$$

where

$$k = \frac{(\gamma + 1)}{\sqrt{2}} \frac{M_\infty^4}{\beta^{3/2}}$$

For a 5/2-power contour, $F(y) = 15/16 \bar{K}y^{5/2}$, where \bar{K} is the proportionality constant to be determined, i.e., $A = \bar{K}x^{5/2}$ is the area growth in terms of the axial variable x . Thus, \bar{K} is given by

$$\bar{K} = \frac{16}{15 kr^{1/2}}$$

and, for $r = 25.4$ cm (10 in.), $\bar{K} = 0.0176 \text{ cm}^{-1/2}$ ($0.028 \text{ in.}^{-1/2}$). A value of $0.0188 \text{ cm}^{-1/2}$ ($0.03 \text{ in.}^{-1/2}$) was selected. The length of the cusp is determined by matching area and slope on the body to which the cusp is fitted if the slope downstream of the matching point is less than that for the 5/2-power contour. For the basic body under consideration, the matching point was selected at a scale length of 1.588 cm (0.625 in.), the slope downstream of this point being less than for the 5/2-power body. The area of the basic body at this point required a total cusp length of 2.945 cm (1.16 in.). Hence, the origin of the basic body modified with the 5/2-power nose cusp is at $x = -1.36$ cm (-0.535 in.). Thus, the basic body contour is given by

$-1.359 \text{ cm} \leq x \leq 1.588 \text{ cm}$ (-0.535 in. $\leq x \leq 0.625$ in.):

$$A_B = 1.88 \times 10^{-2} (x + 1.359)^{5/2} \text{ cm}^2$$

$1.588 \text{ cm} \leq x \leq 3.175 \text{ cm}$ (0.625 in. $\leq x \leq 1.25$ in.):

$$A_B = 1.88 \times 10^{-2} (x + 1/359)^{5/2} - 1.441 \times 10^{-2} (x - 1.588)^{5/2} \\ - 8.94 \times 10^{-2} (x - 1.588)^{3/2} \text{ cm}^2$$

$3.175 \text{ cm} \leq x \leq 19.05 \text{ cm}$ (1.25 in. $\leq x \leq 7.5$ in.):

$$A_B = 0.946 \times 10^{-3} (x + 16.93)^{5/2} - 1.1161 \text{ cm}^2$$

$19.05 \text{ cm} \leq x \leq 25.4 \text{ cm}$ ($7.5 \text{ in.} \leq x \leq 10 \text{ in.}$):

$$A_B = -0.567 \times 10^{-2} (x + 16.93)^3 + 0.591(x + 16.93)^2$$

$$- 19.975(x + 16.93) + 224.354 \text{ cm}^2$$

A.2 Solid Fin

It is required that the Mach-plane area distribution of the fin plus the basic body to which it is attached be equal to that of the $5/2$ -power frontal spike. A double-wedge fin cross-sectional area was selected with straight leading and trailing edges for ease of machining. In addition, in order that the restrictions of slender-body theory not be violated, a maximum lateral flow angle of four degrees was selected. It is also desirable not to allow the fin leading edge to be ahead of the body nose in vertical planes at any point. Moreover, since the maximum cross-sectional width is growing as distance y to the $3/2$ power (Sketch A), the maximum lateral flow angle will occur at the largest value of y for which straight leading- and trailing-edges are maintained. These considerations require that the straight leading- and trailing-edge conditions be abandoned at some point up the fin and the fin width not grow thereafter. The point was selected as $y = 5.69 \text{ cm}$ (2.25 in.). All of these considerations resulted in the following fin design equations:

$0 \leq y \leq 5.69 \text{ cm}$ ($0 \leq y \leq 2.25 \text{ in.}$):

$$h(y) = 0.0195 y^{3/2} \text{ cm}$$

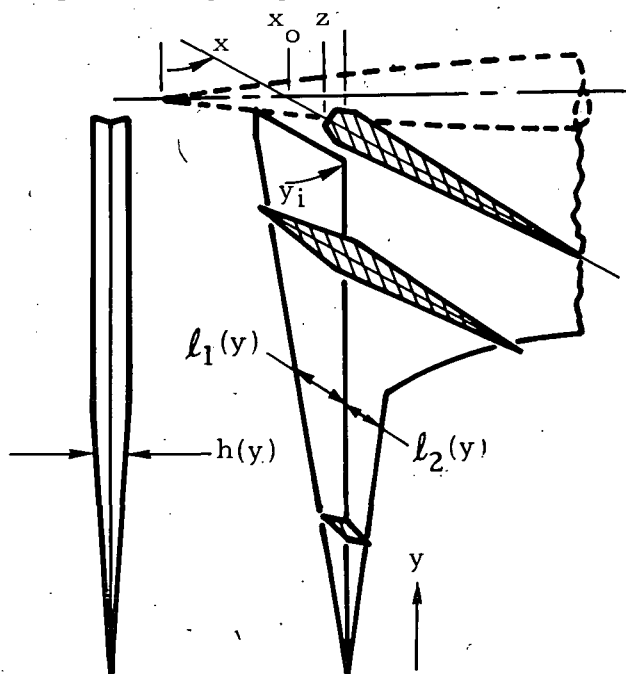
$$\ell_1(y) = 0.476 y$$

$$\ell_2(y) = 0.293 y$$

$5.69 \text{ cm} \leq y \leq y_i$ ($2.25 \text{ in.} \leq y \leq y_i$):

$$h(y) = 0.267 \text{ cm}$$

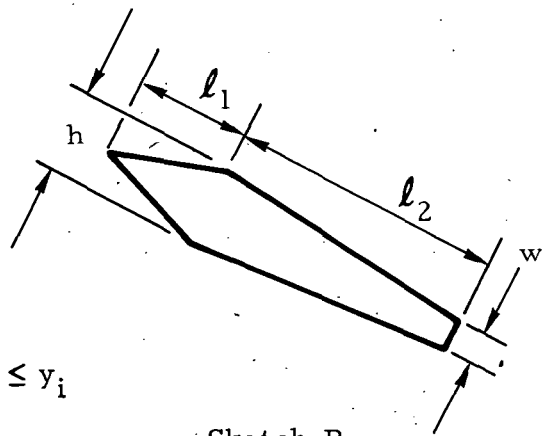
$$\ell_1(y) = \begin{cases} 0.4755 y & \text{if } y \leq 8.61 \text{ cm} \\ 4.1062 \text{ cm} & \text{if } y > 8.61 \text{ cm} \end{cases}$$



Sketch A

$$\ell_2(y) = \begin{cases} \frac{4(A_S - A_B)}{h} - \ell_1, & y \leq 6.769 \text{ cm} \\ 2(y - 5.027), & 6.769 \text{ cm} \leq y \leq y_i \end{cases}$$

$$w = \begin{cases} 0, & y \leq 6.769 \text{ cm} \\ \frac{4(A_S - A_B) - h(\ell_1 + \ell_2)}{2}, & 6.769 \text{ cm} \leq y \leq y_i \end{cases}$$

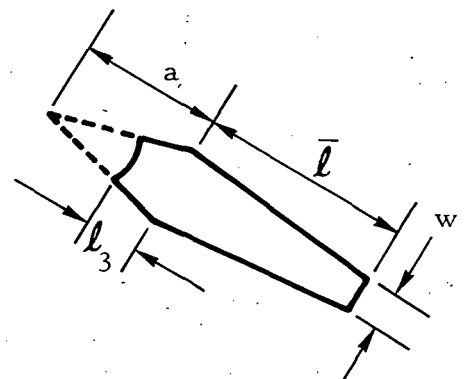


where w is the fin trailing-edge width (Sketch B).

$y_i \leq y \leq y (\ell_3 = 0)$ (Sketch C)

$$\bar{\ell} = 2(y - 5.027) \text{ cm}$$

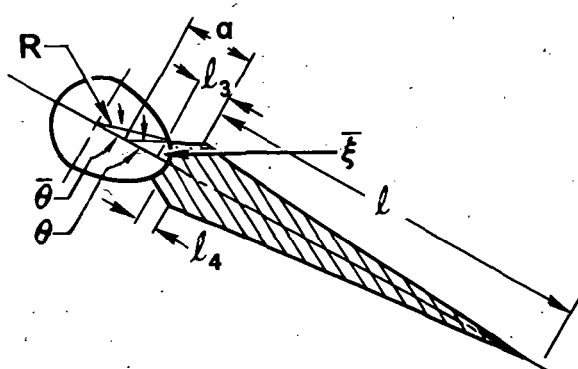
$$w = \frac{2(A_S - A_B) - \frac{ha}{2} \left[1 - (1 - \ell_3/a)^2 \right] + A_{\text{seg}} - h}{\bar{\ell}/2}$$



where $h = 0.267 \text{ cm}$, $a = 4.106 \text{ cm}$ and
 ℓ_3 and A_{seg} are obtained as follows.

Sketch C

To determine ℓ_3



Sketch D

Mach-Plane Cross-Sectional Geometry

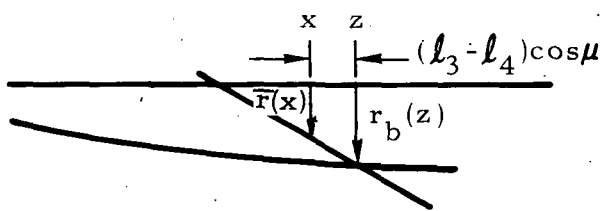
From sketch D

$$\cos \bar{\theta} = \frac{r_b / \sin \mu - (\ell_3 - \ell_4)}{R}$$

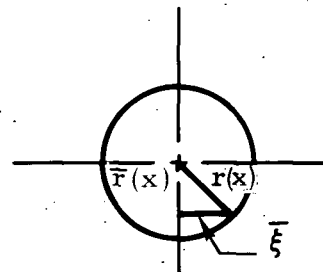
$$\sin \bar{\theta} = \frac{\xi}{R}$$

therefore

$$\bar{\xi}^2 + [r_b / \sin \mu - (\ell_3 - \ell_4)]^2 = R^2 \quad (1)$$



Sketch E1



Plane normal to axis
at $x = z - (\ell_3 - \ell_4)\cos\mu$

Sketch E2

From sketches E1 and E2

$$\bar{r} = [r_b / \sin \mu - (\ell_3 - \ell_4)] \sin \mu \quad (2)$$

$$\bar{\xi}^2 + \bar{r}^2 = r^2 \quad (3)$$

Combining equations (1), (2) and (3)

$$R^2 = \frac{r^2 - \bar{\xi}^2 \cos^2 \mu}{\sin^2 \mu} \quad (4)$$

Also

$$\tan \theta = \frac{\xi}{a - \ell_3} \quad (5)$$

Combining equations (1), (4) and (5)

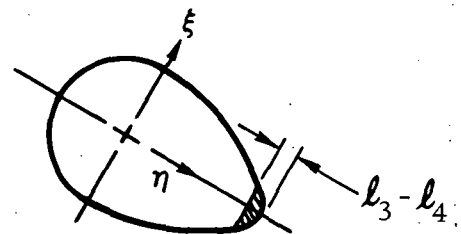
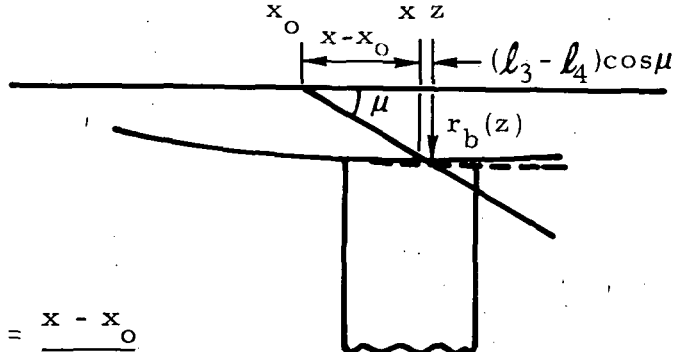
$$\left[a - \ell_4 - (\ell_3 - \ell_4) \right]^2 \tan^2 \theta - r^2(x) + \left[r_b - (\ell_3 - \ell_4) \sin \mu \right]^2 = 0 \quad \left. \begin{array}{l} \\ \Rightarrow \ell_3(z) \\ \text{where } a = 4.106 \text{ cm (1.617 in.)}, \ell_4 = \frac{1-z}{\cos \mu}, \tan \theta = 0.0324 \end{array} \right\}$$

To determine A_{seg}

$$A_{\text{seg}} = 2 \int_{r_b / \sin \mu - (\ell_3 - \ell_4)}^{r_b / \sin \mu} \xi d\eta$$

$$A_{\text{seg}} = 2 \int_{r_b / \sin \mu - (\ell_3 - \ell_4)}^{r_b / \sin \mu} \frac{\sqrt{r^2 - \eta^2 \sin^2 \mu} d\eta}{\sqrt{r^2 - \eta^2 \sin^2 \mu}}, \eta = \frac{x - x_o}{\cos \mu}$$

$$A_{\text{seg}} = \frac{2}{\cos \mu} \int_{z - (\ell_3 - \ell_4) \cos \mu}^z \sqrt{r^2(x) - (x - x_o)^2} \tan^2 \mu dx$$



Simpson's Rule:

$$\int_a^b y dx = \frac{h}{3} \left[y_1 + 4(y_2 + y_4 + \dots + y_n) + 2(y_3 + y_5 + \dots) + y_{n+1} \right], h = \frac{b-a}{n}$$

where $b-a = (\ell_3 - \ell_4) \cos \mu$; let $n=4$, then $h = (\ell_3 - \ell_4) \cos \mu / 4$.

Therefore

$$A_{\text{seg}} = \frac{(\ell_3 - \ell_4)}{6} \left[y_1 + 4(y_2 + y_4) + 2y_3 + y_5 \right]$$

$$y_1 = \sqrt{r^2(x_1) - (x_1 - x_o)^2 \tan^2 \mu} \quad x_1 = z - (\ell_3 - \ell_4) \cos \mu$$

$$y_2 = y(a + h) = y \left[z - (\ell_3 - \ell_4) \cos \mu \left(1 - \frac{1}{4} \right) \right]$$

Therefore

$$y_2 = \sqrt{r^2(x_2) - (x_2 - x_o)^2 \tan^2 \mu}$$

$$y_3 = \sqrt{r^2(x_3) - (x_3 - x_o)^2 \tan^2 \mu}$$

$$x_2 = z - (\ell_3 - \ell_4) \cos \mu \left(1 - \frac{1}{4} \right)$$

$$x_3 = z - (\ell_3 - \ell_4) \cos \mu \left(1 - \frac{1}{2} \right)$$

et cetera. It is now convenient to work in the variable z rather than y .

The following relationships determine the fin design in the range $z(\ell_3 = 0) \leq z \leq 25.4$ cm (10 in.); [$w(x)$, $\ell_2(x)$, $\ell_3(x)$ to be determined]. To determine $\ell_2(x)$

$$x_o = z - r_b \cot \mu \quad (\text{sketch F})$$

The intersection of the Mach planes and axes are given by

$$x_i = \frac{x_o + \sqrt{3}b}{1 - \sqrt{3}a}, \quad y_i = \frac{x_i - x_o}{\sqrt{3}}$$

where $\bar{y} = ax + b$ is the equation of Axis I or II, as appropriate.

$$\text{Axis I: } \bar{y} = 0.1763x - 0.0848 \text{ cm}$$

$$\text{Axis II: } \bar{y} = 0.0782x + 0.214 \text{ cm}$$

Then

$$\ell_2 = \pm \sqrt{(x_i - z)^2 + [\bar{y}_i - r_b(z)]^2}, \quad +: x_i > z \\ -: x_i < z$$

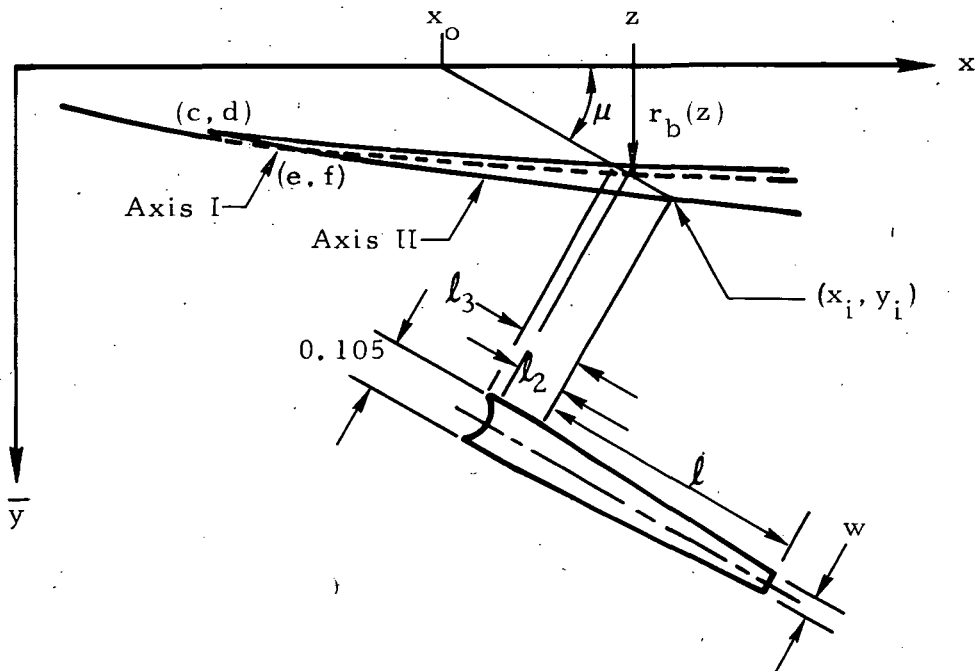
and ℓ_3 is determined by

$$r^2(x) - [r_b(z) - (\ell_3 - \ell_2) \sin \mu]^2 - 0.00696 = 0$$

where $x = z - (\ell_3 - \ell_2) \cos \mu$. The ℓ is given by $\ell = 2(6.215 - y_i)$ cm. Then w is determined from

$$w = \frac{4(A_S - A_B) - 2(h\ell_3 - A_{seg})}{\ell} - h$$

where $h = 0.267$ cm and A_{seg} is determined as before.



$$c = 2.54 \text{ cm} \quad e = 3.045 \text{ cm} \\ d = 0.362 \text{ cm} \quad f = 0.4524 \text{ cm}$$

Sketch F. Design Nomenclature

A.3 Thermal Fin

In each Mach plane, the sum of the fin area plus the effective area due-to-heat plus the basic-body area must equal the 5/2-power frontal spike area distribution, i.e.

$$A_{F\mu} + A_{H\mu} + A_{B\mu} = A_{S\mu}$$

where

$A_{F\mu}$ = fin Mach-plane area due-to-structure

$A_{H\mu}$ = fin Mach-plane area due-to-heat

$A_{B\mu}$ = Mach-plane area due to basic body

$A_{S\mu}$ = Mach-plane area of 5/2-power frontal spike

To accommodate a 0.3175-cm (1/8-in.) diameter nichrome heating tube inside the thermal fin, it was necessary to make this model one and one-half times as large as the solid-fin model. Hence, the basic body portion of the thermal-fin model is given by

$-2.0384 \leq x \leq 2.3813$ cm ($-0.8025 \leq x \leq 0.9375$ in.):

$$A_B(x) = 0.0154 (x + 2.0384)^{5/2} \text{ cm}^2$$

$2.3813 \leq x \leq 4.7625$ cm ($0.9375 \leq x \leq 1.875$ in.):

$$A_B(x) = 0.0154(x + 2.0384)^{5/2} - 0.0118(x - 2.3813)^{5/2} - 0.1091(x - 2.3813)^{3/2} \text{ cm}^2$$

$4.7625 \leq x \leq 28.6$ cm ($1.875 \leq x \leq 11.25$ in.):

$$A_B(x) = 0.00077(x + 25.4)^{5/2} - 0.9896 \text{ cm}^2$$

$2.858 \leq x \leq 38.1$ cm ($11.25 \leq x \leq 15$ in.):

$$A_B(x) = -0.00378(x + 25.4)^3 + 0.591(x + 10)^2 - 29.962(x + 10) + 504.799 \text{ cm}^2$$

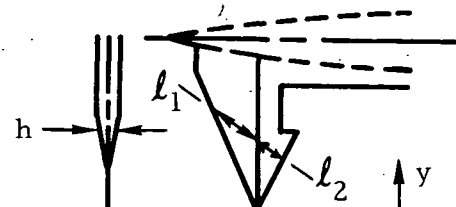
As in the case of the solid fin, it is convenient to work in distance variable y along the fin rather than x (see sketch G). These are related by $y = x/\sqrt{3}$. The design equations for the fin are

$$0 \leq y \leq 8.5725 \text{ cm } (0 \leq y \leq 3.375 \text{ in.})$$

$$h(y) = 0.0159 y^{3/2} \text{ cm}$$

$$\ell_1(y) = 0.4755 y$$

$$\ell_2(y) = 0.2928 y$$



Sketch G

The fin heat starts at $y = 8.58 \text{ cm}$ (3.375 in.). From Appendix B this contribution to the fin area is

$$A_H = 70.452 w^* (y - 8.573) \text{ cm}^2$$

where w^* is the nozzle throat width. Then, in the region $8.573 \leq y \leq 9.254 \text{ cm}$ (3.375 in. $\leq y \leq 3.643 \text{ in.}$):

$$\ell_1 = \ell_1(8.573 \text{ cm}) = -1.536 \text{ cm}$$

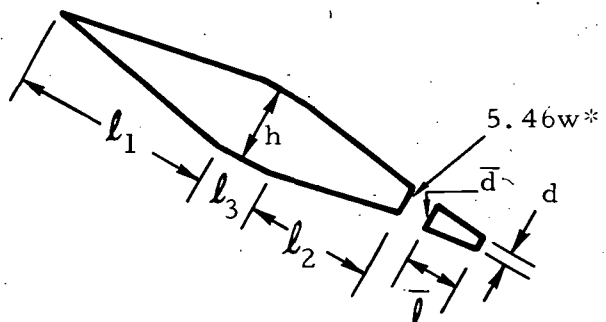
$$\ell_3 = 1.2078 (y - 8.573) \text{ cm}$$

$$\ell = 2.510 - \ell_2 - 2(y - 8.573) \text{ cm}$$

$$h = 0.399 \text{ cm}$$

$$\bar{d} = 5.46w^* - 0.3178(y - 8.573)$$

$$\ell_2 = 2.5103 - 34.3634w^*$$



Sketch H

Then, letting $\bar{d} + d = D$ there is obtained

$$D = \frac{Ky^{5/2} - 0.8129 - 0.1897(y - 8.573) - (0.1994 + 2.73w^*)(2.5103 - 34.3634w^*) - 10.92w^*(y - 8.573)}{17.1817w^* - (y - 3.375)}$$

where $K = 6.11 \times 10^{-3} \text{ cm}^{-1/2}$.

This is of the form $D = N/\bar{D}$; N must be 0 when $\bar{D} = 0$. This is so for

$$w^* = 0.0396 \text{ cm}$$

$$y = 9.253 \text{ cm}$$

Then, $\ell_2 = 1.1473 \text{ cm}$.

The total length of the heated region is given by

$$\frac{A^*}{w^*} = \frac{m/\rho^* V^*}{w^*} = 5.0114 \text{ cm}$$

at the design condition. In $9.253 \text{ cm} \leq y \leq 12.954 \text{ cm}$ ($3.643 \text{ in.} \leq y \leq 5.100 \text{ in.}$)

$$\ell_2 = 1.1473 \text{ cm}$$

$$\ell_1 + \ell_3 = 0.4755 y$$

$$h = 0.399 \text{ cm}$$

The ℓ_1 is given by

$$\frac{h}{2} \ell_1 + h \ell_3 + \left(\frac{h}{2} + 2.73w^* \right) \ell_2$$

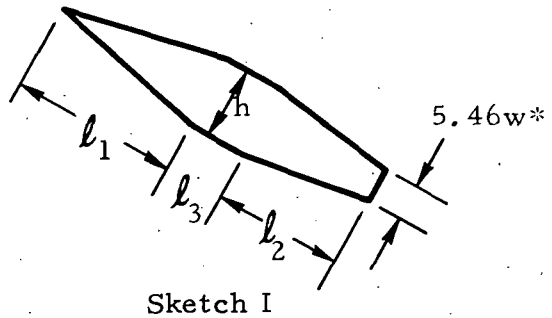
$$+ 10.92w^*(y - 8.573) = Ky^{5/2}$$

At $y = 12.954 \text{ cm}$, $\ell_1 + \ell_3$ becomes constant, and at $y = 13.487 \text{ cm}$, the basic body of revolution begins to contribute to the effective area distribution. Hence, in $12.954 \text{ cm} \leq y \leq 13.487 \text{ cm}$: $\ell_1 + \ell_3 = 6.1595 \text{ cm}$, $\ell_2 = 1.148 \text{ cm}$ and ℓ_1 is determined by the previous expression.

Then, in $12.954 \text{ cm} \leq y \leq 13.584 \text{ cm}$ (end of heated region), ℓ_1 is determined by

$$\frac{h}{2} \ell_1 + h \ell_2 + \left(\frac{h}{2} + 2.73w^* \right) \ell_2 + A_{H\mu} + A_{B\mu} = Ky^{5/2}$$

where $h = 0.399 \text{ cm}$ and $A_{H\mu}$ is given as before.



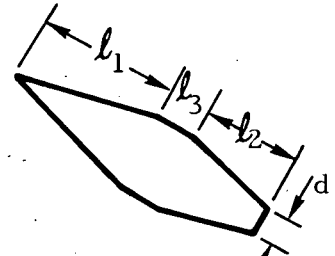
For $y > 13.584$ cm, the heating contribution to the effective area is constant at 2.1697 cm^2 (0.3363 in.^2). The ℓ_2 is allowed to grow linearly and the governing equations are, for $13.584 \text{ cm} \leq y \leq 13.754 \text{ cm}$

$$\ell_1 + \ell_3 = 6.1595 \text{ cm}$$

$$\ell_2 = 1.1473 + 2(y - 13.5834) \text{ cm}$$

$$d/2 = (2.5103 - \ell_2)(0.2017) \text{ cm}$$

$$\frac{h}{2} \ell_1 + h(6.160 - \ell_1) + \left(\frac{h}{2} + \frac{d}{2}\right) \ell_2 + 2.1697 + A_B = Ky^{5/2}$$



Sketch J

where $h = 0.399 \text{ cm}$.

At $y = 13.754$ cm the leading edge of the fin intersects the basic body, and the contribution of the front portion begins to decrease. Thus, in $13.754 \text{ cm} \leq y \leq y(\ell_3 = 0)$ (sketch K)

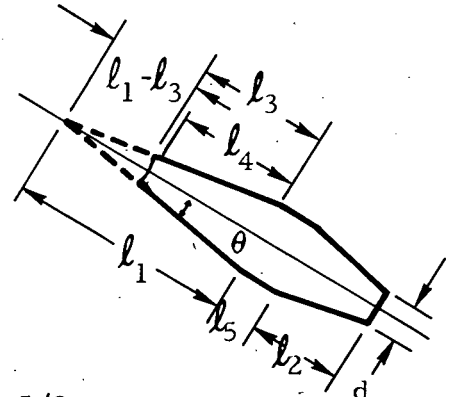
$$\ell_1 = 3.840 \text{ cm}$$

$$\ell_2 = 1.1473 + 2(y - 13.584) \text{ cm}$$

$$\ell_5 = 2.319 \text{ cm}$$

$$h = 0.399 \text{ cm}$$

$$\tan \theta = \frac{h}{2\ell_1} = 0.0519$$



$$\left(\frac{h}{2} + \frac{d}{2}\right) \ell_2 + h\ell_5 + \frac{h}{2} \ell_1 - (\ell_1 - \ell_3)^2 \tan \theta - A_{\text{seg}} = Ky^{5/2}$$

Sketch K

where ℓ_3 and A_{seg} are determined as in the case of the solid fin (see pages 45 through 48).

When the point at which $\ell_3 = 0$ is reached, it is convenient to work in axial variable z rather than normal coordinate y (see page 46). The Mach-plane area distribution in the range $z(\ell_3 = 0) \leq z \leq z(\ell_5 = 0)$ is given by

$$\ell_2 = 1.1473 + 2(y - 13.5834) \text{ cm}$$

$$\ell_6 = (3.81 - z)/\cos \mu = (2/\sqrt{3})(3.81 - z) \text{ cm}$$

$$h = 0.399 \text{ cm}$$

The ℓ_5 is given by

$$\frac{h^2}{4} + [r_b(z) - (\ell_5 - \ell_6) \sin \mu]^2 - r^2(x) = 0$$

where $x = z - (\ell_5 - \ell_6) \cos \mu$. Then w is given by

$$\left(\frac{h}{2} + \frac{w}{2}\right)\ell_2 + h\ell_5 - A_{seg} + 2.1697 + A_{B\mu} = A_{S\mu}$$

In $z(\ell_5 = 0) \leq z \leq 15$, the fin is designed according to the constraints

$$w = \text{const} = 0.465 \text{ cm} [\text{its value at } z(\ell_5 = 0)]$$

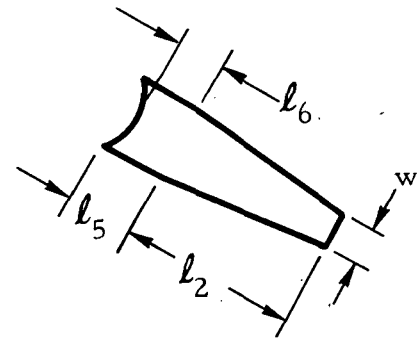
$$\ell_2 = 2[3.856 - r_b(z)] \text{ (bottom edge horizontal)}$$

$\ell - \ell_2$ and h are determined by

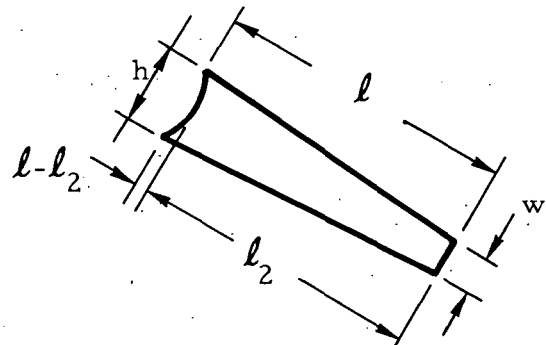
$$\frac{h^2}{4} + [r_b(z) - (\ell - \ell_2) \sin \mu]^2 - r^2(x) = 0$$

where $x = z - (\ell - \ell_2) \cos \mu$

$$(h+w) \left[3.856 - r_b(z) + \frac{\ell - \ell_2}{2} \right] - A_{seg} + 2.1697 + A_{B\mu} = A_{S\mu}$$



Sketch L



Sketch M

A.4 Wing-Body.

It is required that the wing-body combination with wing at angle of attack, α , have the same area distribution as the SST representative equivalent body (fig. 3).

Based on the theory of Polhamus (ref. 17), the total lift of a delta wing is given by the sum of the potential lift and the vortex lift. Accordingly, the lift coefficient is given by

$$C_L = K_p \sin \alpha \cos^2 \alpha + K_v \sin^2 \alpha \cos \alpha$$

where

$$K_p = \frac{\pi AR}{2E}$$

$$K_v = \frac{\pi \sqrt{[16 - (AR\beta)^2][AR^2 + 16]}}{16E^2}$$

The AR is the aspect ratio and E the elliptic integral of the second kind of parameter $m = 1 - (\beta \cot \lambda_{LE})^2$, where $\beta = \sqrt{M_\infty^2 - 1}$, and λ_{LE} is the leading-edge sweep angle.

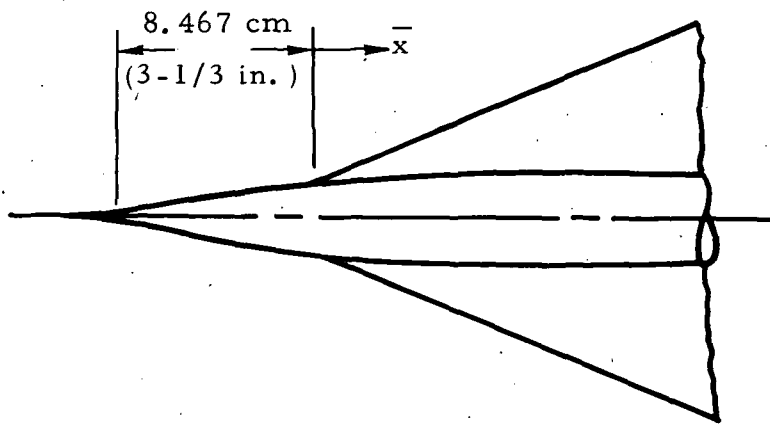
A wing having a root chord of 16.94 cm (6-2/3 in.) was selected (latter two-thirds of body length). It was then necessary to select a sweep angle and angle of attack. For this test, a subsonic leading edge was desired to avoid attached shock waves from the wing. Hence, $\lambda_{LE} > 60$ deg is required for the Mach 2 tunnel flow. The final consideration is that there remain sufficient radius of the basic body at the end of the model to allow support by the sting. On this basis, a 67.5-deg sweep angle and 2/3-deg angle of attack were selected.

The equivalent area due-to-lift is then calculated as a function of running distance, x , from the point of intersection of the wing with the body (sketch M). It is given by

$$A_{eL}(\bar{x}) = \frac{\beta}{\rho_\infty V_\infty^2} L(\bar{x}) = \frac{\beta}{2} C_L S(\bar{x})$$

where $S(\bar{x}) = \bar{x}^2 \tan(\pi/2 - \lambda_{LE}) = 0.414 \bar{x}^2$, for $\lambda_{LE} = 67.5$ deg. Then, for $\alpha = 2/3$ deg, $\beta = \sqrt{3}$

$$A_{eL}(\bar{x}) = 0.008 \bar{x}^2$$



Sketch N

Then, the design condition determining the body shape is

$$A_{BV} + A_{WV} + A_{WL} = A_{BB}$$

where

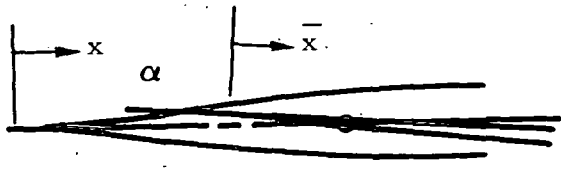
A_{BV} = area of body of wing-body combination due to volume

A_{WV} = area of wing due-to-volume

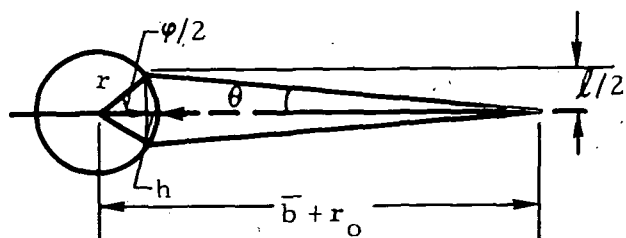
A_{WL} = area of wing due-to-lift

A_{BB} = basic body of revolution area due to volume

Then, defining $A_{BV} = \pi r^2$ and noting other definitions from sketches N and O there is obtained



Sketch O



Sketch P

$$r = \frac{(\bar{b} + r_o) \tan \theta}{\sin(\varphi/2) + \tan \theta \cos(\varphi/2)}$$

$$r^2 + \frac{2(\bar{b} + r_o)r \sin(\varphi/2) - r^2 \varphi}{\cos 40^\circ} + 0.008 \bar{x}^2 = A_{BB}$$

provide two equations for the unknowns r and φ at each value of \bar{x} where

$$\bar{b} = \bar{x} \tan 22.5 \text{ deg}$$

$$r_o = \text{value of } r \text{ at beginning of wing} = 0.785 \text{ cm (0.309 in.)}$$

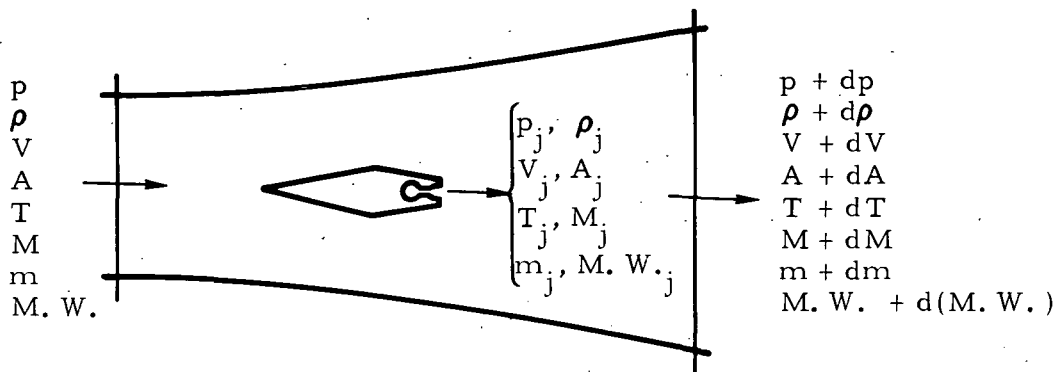
$\tan \theta$ selected at 0.029

$$x = \frac{\bar{x} - 10/3}{\cos 22.5^\circ}$$

APPENDIX B

THERMAL FIN MODEL NOZZLE DESIGN ANALYSIS

The thermal-fin design in Mach planes aft of the point of initiation of the hot gas flow depends on the nozzle design. The nozzle was designed on the basis of one-dimensional flow considerations for flow with mass addition. Consider flow in a streamtube in planes normal to the fin.



The conservation equations for the flow through the streamtube are

$$\text{Continuity: } \frac{m_j}{m} = \frac{d\rho}{\rho} + \frac{dV}{V} + \frac{dA}{A} \quad (B-1)$$

$$\text{where } m_j = \rho_j V_j A_j; \quad m = \rho V A$$

$$\text{Momentum: } (p_j - p)A_j - Adp = mdV + m_j(V - V_j) \quad (B-2)$$

$$\text{Energy: } m(dh + VdV) + m_j \left(h - h_j + \frac{v^2 - v_j^2}{2} \right) = 0 \quad (B-3)$$

$$\text{State: } \frac{dp}{p} = \frac{d\rho}{\rho} + \frac{dT}{T} - \frac{d(M.W.)}{M.W.} \quad (B-4)$$

Combining these equations yields

$$\begin{aligned} \frac{dA}{A_j} &= \frac{\rho_j V_j}{\rho V} \left(1 + \frac{\gamma-1}{2} M^2 \right) \left(\frac{T_j^0}{T^0} + 1 \right) - [1 + (\gamma-1)M^2] \left(\frac{M_j}{M} \right)^2 \frac{p_j}{p} \\ &\quad - \frac{\rho_j V_j}{\rho V} \left(1 - \frac{M.W.}{M.W._j} \right) - \frac{1 + (\gamma-1)M^2}{\gamma M^2} \left(\frac{p_j}{p} - 1 \right) + \frac{1-M^2}{\gamma M^2} \frac{A}{A_j} \frac{dp}{p} \end{aligned} \quad (B-5)$$

where the relationships $V^2/h = (\gamma-1)M^2$, $h^o/h = 1 + (\gamma-1)M_j^2/2$, $h^o/h = 1 + (\gamma-1)M^2/2$ and $d(M.W.)/M.W. = m_j/m_j(1 - M.W./M.W._j)$ have been utilized.

To avoid shock waves in the pressure signature, a nozzle design with $p_j/p = 1$, $dp = 0$ was selected. This reduces equation (B-5) to

$$\frac{dA}{A_j} = \frac{\rho_j V_j}{\rho V} \left(1 + \frac{\gamma-1}{2} M^2 \right) \left(\frac{T_j^o}{T_j^o} + 1 \right) - [1 + (\gamma-1)M^2] \left(\frac{M_j}{M} \right)^2 - \frac{\rho_j V_j}{\rho V} \left(1 - \frac{M.W.}{M.W._j} \right) \quad (B-6)$$

The $\rho_j V_j / \rho V$ can be expressed as

$$\frac{\rho_j V_j}{\rho V} = \frac{M_j}{M} \sqrt{\frac{M.W.}{M.W._j}} \left(\frac{1 + \frac{\gamma-1}{2} M_j^2}{1 + \frac{\gamma-1}{2} M^2} \right)^{1/2} \sqrt{\frac{T_j^o}{T_j^o}} \quad (B-7)$$

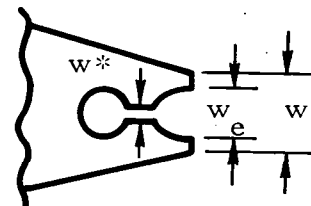
Thus, from equations (B-6) and (B-7)

$$\frac{dA}{A_j} = f \left(M_j, M, \frac{M.W._j}{M.W.}, \frac{T_j^o}{T_j^o} \right)$$

Consideration of possible nozzle exit geometries indicated that an exit-to-throat area ratio $A_e/A^* = 3.5$ and ratio $dA/A_j = 1.56$ appeared practical within the constraints of the external geometry. This fixed $M_j/M = 1.4$ and $T_j^o/T^o = 2.62$ (nitrogen). Under these conditions, the ratio of stagnation pressure in the jet to that in the free stream is $p_j^o/p^o = 3.468$.

Thus, in horizontal planes through the nozzle portion of the thermal fin, the following nozzle exit geometry was chosen:

$$w = \frac{w}{w_e} \cdot \frac{w_e}{w^*} w^* = 1.56 (3.5)w^* \\ = 5.46 w^*$$



The thermal-fin Mach-plane area distribution in the region embodying the nozzle is then given by

$$A_{F_\mu} + \int_{y_i}^y \frac{w(y)dy}{\sin \mu} = Ky^{5/2}$$

where

$A_{F\mu}$ = contribution of solid-fin area to Mach-plane area distribution

$w(y)$ = width of streamtube area due-to-heat as given above

y = distance in vertical direction

y_i = value of y at initial point of heated-gas flow

μ = Mach angle

K = constant = $0.00611 \text{ cm}^{-1/2}$ for thermal fin model 1.5 scale of solid-fin model

For $w = 5.46 w^*$, $\mu = 30 \text{ deg}$, hence

$$A_{F\mu} + 10.92w^*(y - y_i) = Ky^{5/2} \quad (\text{B-8})$$

APPENDIX C

HEATING-TUBE ANALYSIS - DETERMINATION OF NOZZLE MASS-FLOW RATE

From Appendix B, the design condition on the heater is that it delivers gas at the nozzle exit having stagnation temperature

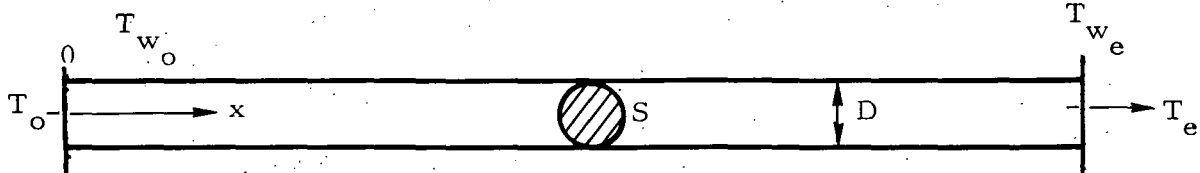
$$T_j^o = 2.62 T^o \quad (C-1)$$

At tunnel operating conditions, $T^o = 570^oR$ (317^oK). Therefore

$$T_j^o = 1492^oR (829^oK)$$

is the required jet stagnation temperature.

The heating-tube design is based on the following analysis. Consider a tube of cross-sectional area S , diameter D , and wall temperature T_w with a gas at temperature T flowing through it.



For heat transfer between the tube wall and the gas the convective heat-transfer coefficient is defined by

$$q_c = hA(T_w - T_b) \quad (C-2)$$

where q_c is the rate of convective heat transfer to the gas in the tube, h is the convective heat-transfer coefficient defined by the above relationship, A is the surface area of the tube, T_w is the wall temperature and T_b the bulk temperature defined by

$$T_b = \frac{\int_0^{r_w} \rho V c_p T 2\pi r dr}{\int_0^{r_w} \rho V c_p 2\pi r dr} \quad (C-3)$$

where ρ is the gas density, V the velocity, c_p the specific heat at constant pressure, and r the radial variable.

For the case of constant-density flow in the tube (low-speed flow) and turbulent pipe flow for which

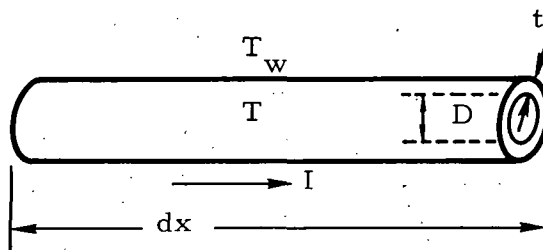
$$\frac{V}{V_c} = \frac{T_w - T}{T_w - T_c} = \left(\frac{r_w - r}{r_w} \right)^{1/7} \quad (C-4)$$

where subscript c denotes centerline values, there is obtained

$$T_b = \frac{1}{6} T_w + \frac{5}{6} T_c \quad (C-5)$$

Thus, to good approximation, $T_b \approx T_c$.

To obtain the relationship between the gas temperature, the wall temperature, the power applied to the tube, and the tube electrical properties, consider the element



Then

$$q_c = h\pi D dx (T_w - T) = \frac{I^2 R}{\pi D t} [1 + \alpha(T_w - T_R)] dx - \epsilon \sigma T_w^4 \pi D dx \quad (C-6)$$

where I is the current, R the resistivity, α a coefficient giving the change of resistivity with temperature, T_R the reference temperature for resistivity, ϵ the wall emissivity, σ the Stefan-Boltzmann constant, D and t the tube diameter and thickness, respectively, and the subscript c has been dropped on the temperature T without loss of generality. The first term on the extreme right-hand side of equation (C-6) represents the heating rate due to resistance, and the second the rate of heat loss due to radiation.

For the nichrome tubing under consideration, $R = 10^{-4}$ ohm-cm (0.3035×10^{-4} ohm-in.) at $293^\circ K$ ($527^\circ R$), $\alpha = 0.0004/\text{ }^\circ K$ ($0.00022/\text{ }^\circ R$), $D = 0.3175$ cm (0.125 in.), $t = 0.0165$ cm (0.0065 in.). At typical operating conditions, $I = 60$ amps, $T_w \approx 1000^\circ K$, and the radiation energy is about 15 percent of the total energy. However, the heating tube will be encased in a

radiation shield and a portion of the radiant energy will be radiated back to it. Thus, neglecting the radiation term there is obtained

$$T = \frac{T_w(\pi Dh - \alpha P) - P(1 - \alpha T_R)}{\pi Dh} \quad (C-7)$$

where $P \equiv I^2 R / \pi D t$.

Now, to obtain the gas temperature as a function of tube length, we make use of the fact that the wall temperature, gas temperature, tube mass-flow rate, and specific heat of the gas are related by

$$\frac{mc}{P} dT = \pi Dh(T_w - T) dx \quad (C-8)$$

Substituting for T_w from equation (C-7) and integrating, there is obtained

$$\frac{x}{D} = \int_{T_0}^T \frac{\frac{mc}{P}}{DP} \frac{1 - \frac{\alpha P}{\pi Dh}}{1 + \alpha(T - T_R)} dT \quad (C-9)$$

where T_0 is the temperature at $x = 0$. The heat-transfer coefficient is given by (ref. 19)

$$Nu_D = \frac{hD}{k} = 0.023 Re_D^{0.8} Pr^{0.4} \quad (C-10)$$

where $Re_D = \rho V D / \mu$ and $Pr = c_p \mu / k$, with ρ being the gas density, V the velocity, μ the viscosity, c_p the specific heat, and k the thermal conductivity. But

$$\rho \bar{V} = \frac{m}{S} \quad (C-11)$$

where S is the cross-sectional area of the tube. Taking the Prandtl number as 0.7, there is obtained

$$\pi Dh \approx 0.1 k^{0.2} \left(\frac{mc}{P} \right)^{0.8} \quad (C-12)$$

In addition, in the range $290^\circ K \leq T \leq 900^\circ K$ ($522^\circ R \leq T \leq 1620^\circ R$), k is given by

$$k = k_o \left(1 + \beta \frac{T - T_o}{T_o} \right) \quad (C-13)$$

where $\beta = 0.56$, $k_o = 2.54 \times 10^{-4}$ (W/cm⁰K) [4.07×10^{-6} (B/ft-sec-⁰R)], Defining $M \equiv mc_p/PD$ and taking $T_R = T_o$ there is obtained from equations (C-9), (C-12) and (C-13)

$$\frac{x}{D} = \frac{M}{\alpha} \ln [1 + \alpha(T - T_o)] - 10\alpha \left(\frac{MP}{k_o} \right)^{0.2} \int_o^{T-T_o} \frac{dt}{(1 + \alpha t) \left(1 + \frac{\beta}{T_o} t \right)^{0.2}} \quad (C-14)$$

where $t \equiv T - T_o$. Equation (C-14) gives the relationship between tube length and gas temperature, T , at the end of that length. Since the flow at that point will be subsonic, $T \approx T_j^o$.

Now, it is desirable to maximize the mass-flow rate in the tube at the design temperature to maximize the amount of fin represented by heat. From the definitions of M and P , it is seen that $M \propto m/I^2$. Hence it is desirable to run the heater at its highest current capability. Moreover, a heating-tube length of 152.4 cm (60 in.) is fixed by the length required through the sting and the amount through the model to the nozzle. For this length, the maximum current is 60 amps. Then

$$\frac{M}{\alpha} = \frac{\pi c_p t m}{I^2 R \alpha} = 96.18 \times 10^4 \text{ cm-sec/kg} (17.14 \times 10^4 \text{ in.-sec/lbm})$$

for nitrogen with $c_p = 0.25$ cal/gm⁰K (0.25 Btu/lbm⁰R) and a heater tube having properties given above. Thus, for $x/D = 152.4 \text{ cm}/0.3175 \text{ cm}$ and $T - T_o = 538^\circ\text{K}$ (970°R)

$$m = 6.52 \text{ gms/sec} (0.0144 \text{ lbm/sec})$$

APPENDIX D

DESCRIPTION OF CONTROL CONSOLE

The controls for operation of the sonic boom test models are located in a self-contained unit shown in figure 30. A schematic diagram and the operating sequence is shown on figures 31 and 32. What follows is a description of the various control functions involved in this unit.

D. 1 Heater Power

The power for the nichrome heater in the model is derived from 240 volt, single phase, 60 cycle service. (208 volt service may be used with a corresponding derating of the unit.) The line voltage is varied with an autotransformer that controls the primary voltage on a two and one-half to one centertapped step-down transformer. This transformer feeds a full wave, silicon rectifier that is filtered with an incandescent light bulb and electrolytic capacitor. Output of 0-50 V dc and 0-100 amps is available at the receptacle on the rear of the cabinet. An interlock is provided on the power system to ensure that the autotransformer is set to zero before the dc power can be turned on.

D. 2 Control Power

Power for all relays and instrumentation is derived from the 240 V ac source through a step-down transformer and a fused 120 V ac circuit. No functions are operational until this circuit is activated as indicated by the white pitot light on the front panel.

D. 3 Actuator Power

Direct current for the motor which drives the model sting is obtained from a full wave bridge rectifier and a dropping rheostat (for speed control). Local setting of speed and direction is possible with controls on the front panel. Remote actuation (at full speed) is provided by relays that are energized through a three-pin receptacle at the rear of the unit. (115 V ac relays are installed, but other voltages may be used by replacing K2 and K3 with octal base relays of appropriate coil voltages.)



Figure 30. Sonic-Boom Control Console

1/4 O.D. 0.019W 304 E.S. TUBING
WITH 1/4 SWAGELOK FITTINGS

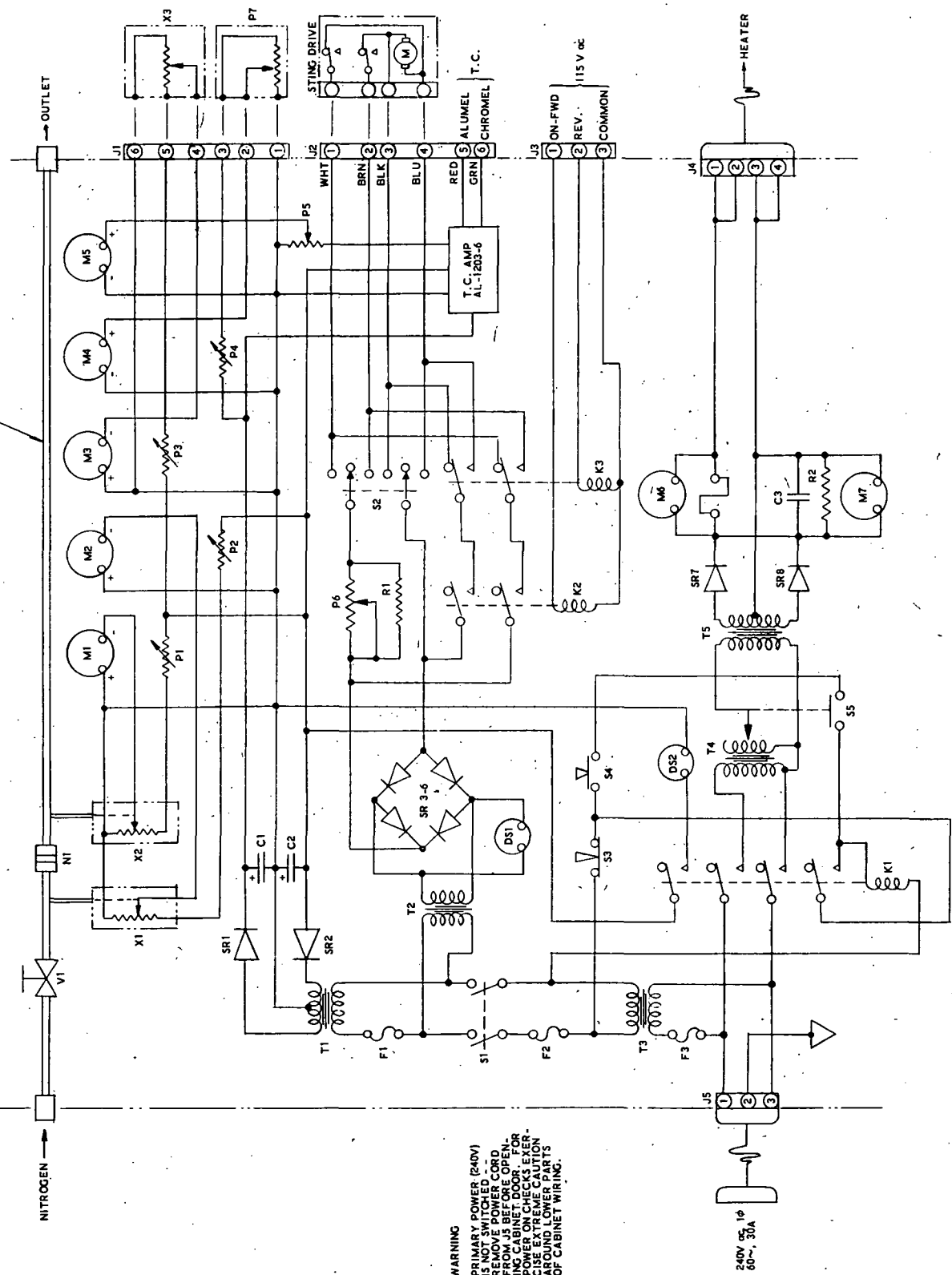


Figure 31. Sonic-Boom Test Console Schematic

LEGEND

CODE	DESCRIPTION	FUNCTION/PANEL LABEL(S)	OPERATION
S1	DPST, ISA	<u>CONTROL POWER ON-OFF</u>	1. VERIFY THROTTLE VALVE (V1) IS CLOSED DO NOT OVER TIGHTEN
S2	DPDT, CTR OFF, 15A	<u>FWD-REV</u>	2. MAKE ALL SERVICE CONNECTIONS TO VARIOUS RECEPTACLES/FITTINGS
S3	SPST, N.C. MOM	<u>HEATER ON</u>	3. TURN ON CONTROL POWER (S1)
S4	SPST, N.O. MOM	<u>HEATER OFF</u>	4. ZERO ALL METERS WITH SCREW ADJUSTMENT ON METER FACE
S5	SPST, N.O. MOM	HEATER INTERLOCK	5. IF METERS ARE TO BE CALIBRATED, APPLY SIGNALS AND ADJUST RANGE (P1-S), RE- ZERO AND READJUST RANGE AS REQUIRED
V1	WHITEY IR54-3/16	THROTTLE VALVE	6. OPEN THROTTLE VALVE TO SET PROPER NITROGEN FLOW RATE. DO NOT EXCEED XDCR RANGE (X1-3)
N1	CAJON 8 V c + AL-3158-19	METERING NOZZLE	7. FOR PROPER METERING M2>2 X M1. IF THIS DOES NOT OBTAIN, CHANGE METERING NOZZLE (N1) TO SMALLER SIZE
X1	BOURNS XDCR	SUPPLY PRESSURE	8. VERIFY HEATER CONTROL (T4) IS SET AT ZERO, TURN ON HEATER (S4) AND RAISE TO REQUIRED POWER LEVEL AS SHOWN ON M6 AND M7
X2	BOURNS XDCR	HEATER PRESSURE	9. MOVE STING WITH ACTUATOR CONTROL FWD/REV. (S2) AND ADJUST SPEED (P6) AS REQUIRED. REMOTE CONTROL THRU J3 -- FULL SPEED ONLY
X3	BOURNS XDCR	NOZZLE PRESSURE	10. MONITOR SUPPLY PRESSURE (M2). IF IT FALLS BELOW SET LEVEL, VERIFY SAFE NOZZLE TEMP (M5) OR REDUCE POWER
P1-4	500Ω , 0.2W	RANGE ADJUST	11. FOR SHUTDOWN, REDUCE HEATER CONTROL TO ZERO. CONTINUE GAS FLOW TO COOL HEATER AND STING/MODEL HDWE
P5	20KΩ , 0.2W	RANGE ADJUST	12. TURN OFF HEATER (S3) AND CONTROL POWER (S1).
P6	50Ω , 2W	ACTUATOR <u>SPEED</u>	
R1	25Ω , 2W	SPEED RANGE	
R2	100W BULB	LEAK RESISTER	
C1,2	100 μF , 25V	FILTER CAPACITOR	
C3	0.044F , 75 W V dc	FILTER CAPACITOR	
IN540		15 V dc SUPPLY	
SR1,2	IN4004	12 V dc SUPPLY	
SR3-6	AMD 450 F100R	HEATER DC	
SR7,8	TRIAD F-91X	40 V ct XFR	
T1	TRIAD F-26X	12.6 V XFR	
T2	WESCO 1741-220	23/115 CONTROL XFR	
T3	GR VARIAC W20G2	<u>HEATER CONTROL</u>	
T4	BURTON 240 V 2.5:1 CT	POWER XFR	
T5	STARTER, SIZE 1, 20A	LINE RELAY	
K1	P B KPR, 120 V ac	REMOTE STING CONTROL	
K2,3	FUSE, 1/4 A	15 V dc OVERLOAD	
F1	FUSE, 1/2 A	12 V dc OVERLOAD	
F2	FUSE, 1 A	115 V ac OVERLOAD	
F3		HEATER PRESSURE SUPPLY PRESSURE	
M1	0-10 V dc, 0-500 psig	NOZZLE PRESSURE	
M2	0-10 V dc, 0-1000 psig	ACTUATOR POSITION	
M3	0-10 V dc, 0-200 psig	NOZZLE TEMPERATURE	
M4	0-10 V dc, 0-100%	HEATER CURRENT	
M5	0-10 V dc, 0-1000°K	HEATER VOLTAGE	
M6	0-100 AMP DC	STING INSTRUMENTATION	
M7	0-50 V dc	ACTUATOR POWER	
J1	CANNON WK-6-315	REMOTE STING CONTROL	
J2	CANNON WK-6-315	OUTPUT	
J3	HUBBELL NO. 7301	240 VAC SOURCE	
J4	HUBBELL NO. 7958	CONTROL POWER ON	
J5	WHITE, NO. 1813	HEATER POWER ON	
DS1	RED, NO. 1813		
DS2			

Figure 32. Sonic-Boom Test Console Legend
and Operating Instructions

D.4 Gas Supply

Nitrogen for the heater is controlled by a throttling valve that operates on a gas supplied at a regulated, constant pressure. A sonic orifice is used for metering the flow so a pressure ratio of at least two must be maintained at all times between "supply" and "heater" pressure.

D.5 Instrumentation

All system parameters are measured and displayed on meters on the front panel. No recorder connections are provided. Power for transducers is furnished from a ± 20 V dc, filtered, one-half wave rectifier. Pressure and position transducers are potentiometer devices. Nozzle temperature is measured with a chromel-alumel thermocouple, the output of which is amplified in an integrated circuit unit for direct reading on the panel meter.

REFERENCES

1. Batdorf, S. B.: Alleviation of the Sonic Boom by Thermal Means. *Journal of Aircraft*, vol. 9, no. 2, February 1972, pp. 150-156.
2. Seebass, R. and George, A. R.: Sonic-Boom Minimization. *Journal of the Acoustical Society of America*, vol. 51, no. 2 (Part 3), February 1972, pp. 686-694.
3. Hubbard, Harvey H. and Mayes, William H.: Sonic Boom Effects on People and Structures. *Sonic Boom Research*, A. R. Seebass, Ed., NASA SP-147, 1967, pp. 65-76.
4. Hayes, Wallace D. and Weiskopf, Francis B., Jr.: Optimum Configurations for Bangless Sonic Booms. *Quarterly of Applied Mathematics*, vol. 30, no. 3, October 1972, pp. 311-328.
5. George, A. R. and Seebass, R.: Sonic-Boom Minimization Including Both Front and Rear Shocks. *AIAA Journal*, vol. 9, no. 10, October 1971, pp. 2091-2093.
6. McLean, F. Edward: Configuration Design for Specified Pressure Signature Characteristics. *Second Conference on Sonic Boom Research*, I. R. Schwartz, Ed., NASA SP-180, 1968, pp. 37-45.
7. Cheng, S. I. and Goldburg, A.: An Analysis of the Possibility of Reduction of Sonic Boom by Electro-Aerodynamic Devices. *AIAA Paper No. 69-38*, New York, January 1969.
8. Miller, David S. and Carlson, Harry W.: Application of Heat and Force Fields to Sonic-Boom Minimization. *Journal of Aircraft*, vol. 8, no. 8, August 1971, pp. 657-662.
9. Lippert, F. W.: An Analytical Study of Some Possible Sonic Boom Alleviation Schemes. *AIAA Paper No. 72-653*, Boston, June 1972.
10. Cahn, M. S. and Andrew, G. M.: *Electroaerodynamics in Supersonic Flow*. AIAA Paper No. 68-24, New York, 1968.
11. Ferri, A.: Airplane Configurations for Low Sonic Boom. *Third Conference on Sonic Boom Research*, I. R. Schwartz, Ed., NASA SP-255, 1971, pp. 255-275.
12. Mechtly, E. A.: The International System of Units of 1960-Physical Constants and Conversion Factors. *NASA SP-7012*, 1964.
13. Carlson, Harry W.: Experimental and Analytic Research on Sonic Boom Generation at NASA. *Sonic Boom Research*, A. R. Seebass, Ed., NASA SP-147, 1967, pp. 9-23.

REFERENCES (Continued)

14. Carlson, Harry W., Mack, Robert J., and Morris, Odell A.: A Wind-Tunnel Investigation of the Effect of Body Shape on Sonic-Boom Pressure Distributions. NASA TN D-3106, November 1965.
15. Carlson, H. W. and Morris, O. A.: Wind-Tunnel Sonic-Boom Testing Techniques. Journal of Aircraft, vol. 8, no. 3, May-June 1967, pp. 245-249.
16. Lomax, H.: The Wave Drag of Arbitrary Configurations in Linearized Flow as Determined by Areas and Forces in Oblique Planes. NACA RM A55A18, January 1955.
17. Whitham, G. B.: The Flow Pattern of a Supersonic Projectile. Communications on Pure and Applied Mathematics, vol. 5, 1952, pp. 301-348.
18. Polhamus, E. C.: Prediction of Vortex-Lift Characteristics Based on a Leading-Edge Suction Analogy. AIAA Paper 69-1133, October 1969.
19. McAdams, W. H.: Heat Transmission. McGraw-Hill, 1954, pp. 205-250.

NATIONAL AERONAUTICS AND SPACE ADMINISTRATION
WASHINGTON, D.C. 20546

OFFICIAL BUSINESS
PENALTY FOR PRIVATE USE \$300

SPECIAL FOURTH-CLASS RATE
BOOK

POSTAGE AND FEES PAID
NATIONAL AERONAUTICS AND
SPACE ADMINISTRATION
451



POSTMASTER : If Undeliverable (Section 158
Postal Manual) Do Not Return

"The aeronautical and space activities of the United States shall be conducted so as to contribute . . . to the expansion of human knowledge of phenomena in the atmosphere and space. The Administration shall provide for the widest practicable and appropriate dissemination of information concerning its activities and the results thereof."

—NATIONAL AERONAUTICS AND SPACE ACT OF 1958

NASA SCIENTIFIC AND TECHNICAL PUBLICATIONS

TECHNICAL REPORTS: Scientific and technical information considered important, complete, and a lasting contribution to existing knowledge.

TECHNICAL NOTES: Information less broad in scope but nevertheless of importance as a contribution to existing knowledge.

TECHNICAL MEMORANDUMS: Information receiving limited distribution because of preliminary data, security classification, or other reasons. Also includes conference proceedings with either limited or unlimited distribution.

CONTRACTOR REPORTS: Scientific and technical information generated under a NASA contract or grant and considered an important contribution to existing knowledge.

TECHNICAL TRANSLATIONS: Information published in a foreign language considered to merit NASA distribution in English.

SPECIAL PUBLICATIONS: Information derived from or of value to NASA activities. Publications include final reports of major projects, monographs, data compilations, handbooks, sourcebooks, and special bibliographies.

TECHNOLOGY UTILIZATION PUBLICATIONS: Information on technology used by NASA that may be of particular interest in commercial and other non-aerospace applications. Publications include Tech Briefs, Technology Utilization Reports and Technology Surveys.

Details on the availability of these publications may be obtained from:

SCIENTIFIC AND TECHNICAL INFORMATION OFFICE

NATIONAL AERONAUTICS AND SPACE ADMINISTRATION

Washington, D.C. 20546